UNIVERSITY
OF OSLO

Master's thesis

Ionospheric Ion Composition Changes During Geomagnetic Storms

A study utilizing Swarm's SLIDEM product to determine ionospheric changes in the effective ion mass

Martin André Helvig

Plasma and Space Physics
30 ECTS study points

Department of Physics
Faculty of Mathematics and Natural Sciences

Spring 2023

Martin André Helvig

Ionospheric Ion Composition Changes During Geomagnetic Storms

A study utilizing Swarm's SLIDEM product to determine ionospheric changes in the effective ion mass

Supervisor:
Lasse Clausen

Abstract

A geomagnetic storm originates from high-energy solar events, e.g. a coronal mass ejection, causing massive solar winds leading to complex disturbances and changes to the near-Earth space environment. This master's thesis is a study of the changes to the ionospheric ion composition during geomagnetic storms. Four selected geomagnetic storm events have been investigated using the data produced by the newly developed Swarm Langmuir probe Ion drift, Density and Effective Mass (SLIDEM) product. The thesis' hypothesis is that the increase in energy from the geomagnetic event will lead to observable changes in the ion composition at Swarm altitudes. Observations of the Effective Ion Mass, M_{eff}, reveal a tendency of a greater fraction of heavy ions during storm time. However, the four storms unveil diverse observations giving rise to an interesting discussion.

Acknowledgment

First of all, I want to express my gratitude to the Creator, for creating this extravagant universe for us to live in, experience, and explore. Secondly, I want to thank Lasse Clausen for his patient guidance through the rewarding experience of writing this master's thesis. I also want to give thanks to Kristoffer Falk Austnes, my brother-in-arms. If not for you, I would not even have considered writing my master's thesis in Space Physics, or gotten to know all the wonderful people in 4DSpace. A special thanks must also be given to Lisa who made Space Waffles every first Friday of the month.

Lastly, I want to thank my friends and family, especially my wife, for cheering me on through the ups and downs. I would not have survived the final few weeks of writing this thesis without her making sure I got enough sleep, food, and encouragement.

Contents

List of Figures

List of Tables

Chapter 1

Introduction

Geomagnetic storms have fascinated mankind for thousands of years with their beautiful auroras (NASA, 2006). The knowledge of these phenomena has grown rapidly over the last couple of centuries. There are still many concepts and complexities that are yet to be understood, giving opportunities for continued investigations of geomagnetic storms and their impacts.

A key aspect of science is the ability to make accurate measurements. When studying a geomagnetic storm and its interactions with different parts of the Earth's space environment, having reliable measurements of the different parameters connected with a storm would increase the possibility of learning something new. Modern technology has made way for new and precise methods of measuring, e.g. satellites. The ability to measure aspects of the magnetosphere or ionosphere directly from within is a huge development in space physics research.

Swarm is a satellite constellation whose main goal is to measure the Earth's magnetic field, but also has plasma instruments for measuring key ionospheric parameters, like density, and ion flow, among other things (Pakhotin et al., 2022). As the low latitude ionosphere experiences several different density and composition changes, Swarm measurements can be used to get a better understanding of these phenomena. Examples of such would be the Appleton anomaly (Appleton, 1946), F-region dynamo (Rishbeth, 1981), plasma bubbles (Woodman & La Hoz, 1976), etc. However, other space weather phenomena, like the evolution of the ring current (Ganushkina et al., 2015), would also benefit greatly from accurate ion composition measurements. Swarm satellites do not have a mass spectrometer as one of their instruments, so a composition of 100 % O^+-ions is often assumed. To relax these assumptions Pakhotin et al. (2022) developed a method called the Swarm Langmuir Probe Ion Density and Effective Mass (SLIDEM) that determines an ion fraction, or effective ion mass (M_{eff}), sensitive to the presence of lighter ions in the ionosphere.

A complete Swarm historical data set has been produced and is made available for further research. Being fairly new, limited research has been done using the SLIDEM data. Therefore, the main objective of this thesis is to use the historical SLIDEM data to investigate ionospheric ion composition changes in response to geomagnetic storms, by analyzing the data associated with four selected storm events.

This thesis is divided into six chapters. Chapter two presents general theory of space physics, the Sun and the solar wind, the magnetosphere and the ionosphere. It also outlines what a geomagnetic storm is and how it is measured, and how energy is transported into the ionosphere. The third and fourth chapters describe what the Swarm constellation and the SLIDEM product are. These chapters include a description of the data and methodology used for the thesis, and present the observations done throughout this project. Chapter five discusses the findings in relation to existing knowledge. It further covers a discussion regarding the usage of the SLIDEM product and its capabilities and deficiencies. Lastly, the thesis will be summarized in a conclusion and an outlook toward possible succeeding studies.

Chapter 2

Theory

This chapter contains the theoretical basis on which the thesis will be structured upon. Firstly, some plasma physics and magnetohydrodynamics will be introduced as it is the basis of understanding the coupling between the solar wind and Earth's magnetosphere. Following this, theory on the Sun and the solar wind, the magnetosphere, the ionosphere, and how these are coupled together, is described. In the final part of this chapter, a definition of a geomagnetic storm will be presented along with two means of measurement, and some consequences in energy transport succeeding a geomagnetic storm.

2.1 Plasma Physics

Plasma is described as the fourth state of matter and is defined as a hot, quasineutral gas that consists of charged and neutral particles with a collective behavior (Chen, 2016). Quasineutrality is achieved when the number of electrons equals the number of ions in the gas, $n_e = n_i$ (Pecseli, 2020). In other words, the net charge of the plasma is zero.

Plasma behavior is often described using three methods; single-particle motion, magnetohydrodynamics (MHD), and kinetic theory. The first describes the trajectories of single particles in a plasma, disregarding collective behavior. The kinetic theory uses the assumption that particle velocities are Maxwellian, making it possible to trace each individual particle and how they interact with each other. This method is generally used on smaller samples of plasma as it depends on a high amount of computation (Pecseli, 2020). In MHD, plasma is considered a fluid, hence fluid mechanics can be used to describe the collective behavior of the plasma. In this thesis, plasma will be described with the MHD model, but in order to adequately describe it, some concepts from single-particle motion will be introduced.

In single-particle motion, the equation of motion for a charged particle in the presence of an electric and magnetic field is given by

$$\vec{F} = q(\vec{E} + \vec{v} \times \vec{B}) \tag{2.1}$$

where $\vec{F}$ is the force, q is the charge of the particle, $\vec{E}$ is the electric field, $\vec{B}$ is the magnetic field, and $\vec{v}$ is the velocity of the particle. This equation is a combination of Newton's 2nd law, $\sum \vec{F} = m\vec{a}$, the Coulomb force, $\vec{F_C} = q\vec{E}$, and the Lorentz force, $\vec{F_L} = q(\vec{v} \times \vec{B})$ (Chen, 2016; Pecseli, 2020). It can be used to predict the complex motion

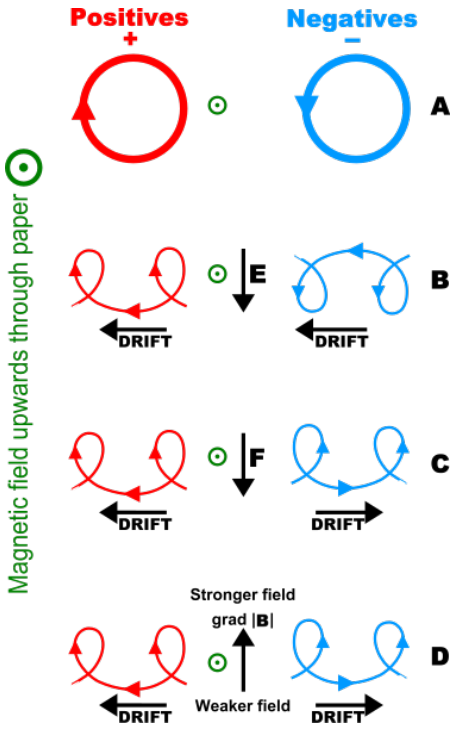

Figure 2.1: Motion and drifts of single particles. (A) show the gyromotion for charged particles in a homogeneous magnetic field (pointing out of the paper) where no electric fields or external forces are present. (B) show the gyration and drift when charged particles are in a magnetic and electric field (pointing downwards), (C) is when acted upon by an external force (pointing downward), e.g. gravity, and (D) shows the motion when inside a magnetic field with a gradient in field strength (pointing upwards).

patterns charged particles can exhibit when inside a magnetic field. An important assumption for this model is that the density of the charged particles is low, hence they do not interact with each other, and only the background magnetic and electric fields influence the motion. If a charged particle moves in a homogeneous magnetic field without any external forces or electric fields, the particle will gyrate due to the Lorentz Force, $\vec{F}_L = q(\vec{v} \times \vec{B})$. As seen in figure (2.1A) a negatively charged particle will gyrate in the opposite direction of a positively charged particle. In the presence of an electric and magnetic field, the particle will be accelerated with or against the electric field depending on its charge. The resulting velocity will then lead to a gyrating motion but as the particle gyrates, it will be decelerated by the electric field. This will produce a drifting motion. Since the force from the electric field and the Lorentz force depends on the charge, all charged particles will drift in the same direction. This can be seen in (2.1B). In the presence of an external force, a similar drift as the one just explained will occur. However, since the force will accelerate negative and positive charges in the same direction, the drift will be in opposite directions (figure 2.1C). Another type of drift motion occurs when a charged particle moves into a nonuniform magnetic field with a strength gradient. As the particle gyrates, it moves into regions of different magnetic field strengths, and its gyro-radius changes depending on its position in the field. This change in the gyro-radius causes a drifting motion of the particle, as shown in figure (2.1D).

Some characteristic parameters for plasma are the Debye length, λ_D, which is:

$$\lambda_D = \sqrt{\frac{\epsilon_0 k_B T}{e^2 n}} \tag{2.2}$$

where ϵ_0 is the vacuum permeability, k_B is the Boltzmann constant, T is the temperature, e is the electric charge, and n is the density (Chen, 2016). This length can be defined as the length a plasma particle travels within one plasma period, τ_p, which is another parameter:

$$\tau_p = \frac{2\pi}{\omega_{pe}} \tag{2.3}$$

where the plasma frequency, ω_{pe} is:

$$\omega_{pe} = \sqrt{\frac{e^2 n_e}{\epsilon_0 m_e}} \tag{2.4}$$

where n_e and m_e are the electron density and mass, respectively (Chen, 2016). Another plasma parameter is the plasma beta, β, which is the ratio between the thermal pressure and the magnetic field pressure. A highβ is common in plasma described using MHD, which will be explained in more detail later (Pecseli, 2020).

Plasma can not simply be understood as single particles since they will interact with each other resulting in a collective behavior. That is why the MHD description is useful when modeling large-scale plasma. Magnetohydrodynamics is the study of the behavior of electrically conductive fluids and is, for instance, used to describe fully ionized plasma (Pecseli, 2020). Requirements for using the MHD description are that the characteristic scale length and time of the fluid are much larger than the Debye length and plasma period (Pecseli, 2020). This thesis is mainly investigating ionospheric plasma where the density is typically in the 10^5 cm^{-3} scale and the temperature is between $1000 - 1500$ K. From the equations this gives a λ_d in cm and an ω_{pe} in MHz resulting in a τ_p in μs (Darian et al., 2017). As the data used in this thesis is on a much larger length and time scale, the MHD description is considered safe to use.

Fully ionized plasma can be found in various regions of space, including the Earth's ionosphere and magnetosphere (Pecseli, 2020; Russell et al., 2016). The MHD equations for simple incompressible, ideal MHD are obtained using the equation of motion and Maxwell's equations for magnetized plasma. These equations describe the behavior of the magnetic field, bulk flow velocity, plasma density, and plasma pressure. The equations are as follows:

$$\frac{\partial \vec{B}}{\partial t} = \nabla \times (\vec{u} \times \vec{B}) \tag{2.5}$$

$$\frac{\partial \rho}{\partial t} + \vec{u} \cdot \nabla \rho = 0 \tag{2.6}$$

$$\nabla \cdot \vec{u} = 0 \tag{2.7}$$

$$\rho \left(\frac{\partial \vec{u}}{\partial t} + \vec{u} \cdot \nabla \vec{u} \right) = -\nabla p + \frac{1}{\mu_0} \left(\nabla \times \vec{B} \right) \times \vec{B} \tag{2.8}$$

where $\vec{B}$ is the magnetic field, $\vec{u}$ is the bulk flow velocity, ρ is the plasma density, p is the plasma pressure, and μ_0 is the permeability constant (Pecseli, 2020).

Some assumptions must be made when dealing with the MHD model. Firstly, the plasma is assumed to be describable as a single fluid which is a characteristic of high-conductivity plasma. Secondly, the plasma species; electrons and ions, are both assumed to have an equal temperature. This, together with the quasi-neutrality, means that the pressure is the same. Lastly, the plasma must be in thermal equilibrium, meaning that the distribution function of particle velocities in a small volume in the plasma is locally Maxwellian (Pecseli, 2020).

With MHD covered, an important phenomenon for plasma in space, the frozen-in theorem, can be explained. When dealing with ideal MHD, the conductivity of the plasma goes toward infinity. This theorem states that magnetic fields in the plasma move as if frozen into the plasma (Pecseli, 2020). A visual representation is seen in figure (2.2), where plasma is shown as a white cloud and magnetic field lines are the black arrows frozen into the plasma cloud. If the plasma cloud moves, the magnetic field lines will be dragged along with it, and if the magnetic field lines move, the plasma will be pulled after as the magnetic field lines want to be straightened out.

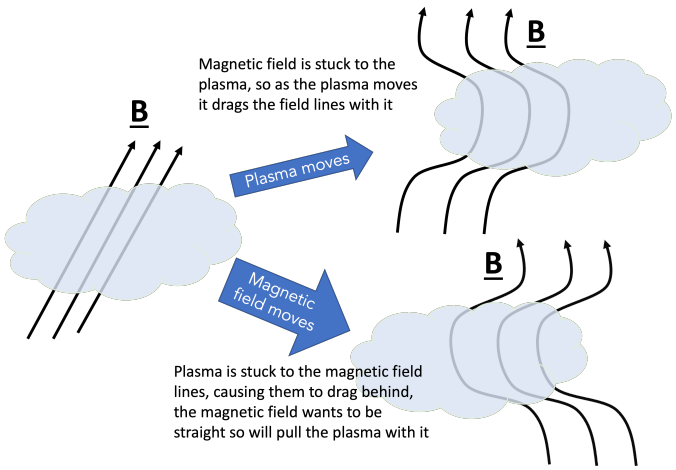

Figure 2.2: Visual explanation of the frozen-in theorem. Credit: SuperDARN (2023)

There is a possibility of the frozen-in theorem breaking down. This happens when antiparallel magnetic field lines are pushed towards each other until they eventually break apart and reconnect with each other, as seen in figure (2.3). The northward magnetic field lines (blue) and the southward magnetic field lines (red) are pushed toward each other by an external force (black arrows 2.3a). At one point the field lines will break and reconnect with the opposite field line, releasing stored energy in the magnetic field line as heat or kinetic energy (black arrows 2.3c) (Priest & Forbes, 2000; Russell et al., 2016). Reconnection is an important feature of how energy from the solar wind is dispatched into the Earth's atmosphere and will be explained in detail later (section 2.5).

With some basic concepts of plasma physics fresh in mind, the chapter will proceed to a section on the Sun and the solar wind, followed by theory on the magnetosphere and ionosphere, before the chapter rounds up with a section on the couplings between the two layers.

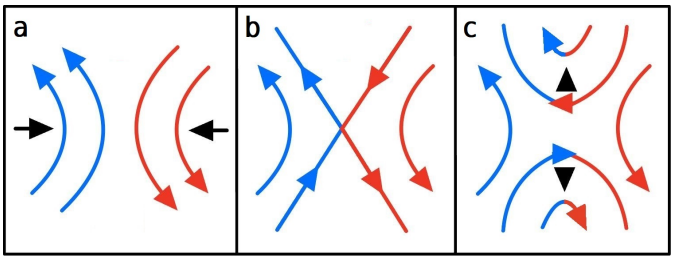

Figure 2.3: Antiparallel magnetic field lines (red and blue arrows) are being pushed together by an external force (black arrows in (a)) forcing them to reconnect with each other.

2.2 The Sun and Solar Wind

As the name implies, the Sun is the driver of the solar wind. Through nuclear reactions in the Sun's core, a vast amount of energy is produced and transported out to the outer layers of the Sun. The energy build-up results in massive amounts of high-energy particles, plasma, being flung into space. As this plasma is highly conductive, the Sun's magnetic field lines are frozen-in with the plasma (Pecseli, 2020). When the plasma travels outwards from the Sun, the magnetic field lines will travel with it. These field lines form a field called the Interplanetary Magnetic Field (IMF) (Russell et al., 2016). As the IMF travels with the solar wind, it takes the shape of spirals, as seen in figure (2.4). This is caused by the rotation of the Sun and the fact that the magnetic field lines are still connected to the Sun. This shape is called the Parker spiral (Russell et al., 2016). The solar wind, on the other hand, travels radially away from the Sun. The traveling speed depends on the solar activity that caused the plasma to be launched from the Sun's surface but averages around 400-500 km/s. During significant events, like a coronal mass ejection, the speed could exceed 1000 km/s, while during a solar minimum, the speed could be as low as 300 km/s (NASA, 2014). The difference in speed could lead to compression regions as the fast-moving solar wind catches up with and collides with the slower solar wind, as seen in figure (2.4).

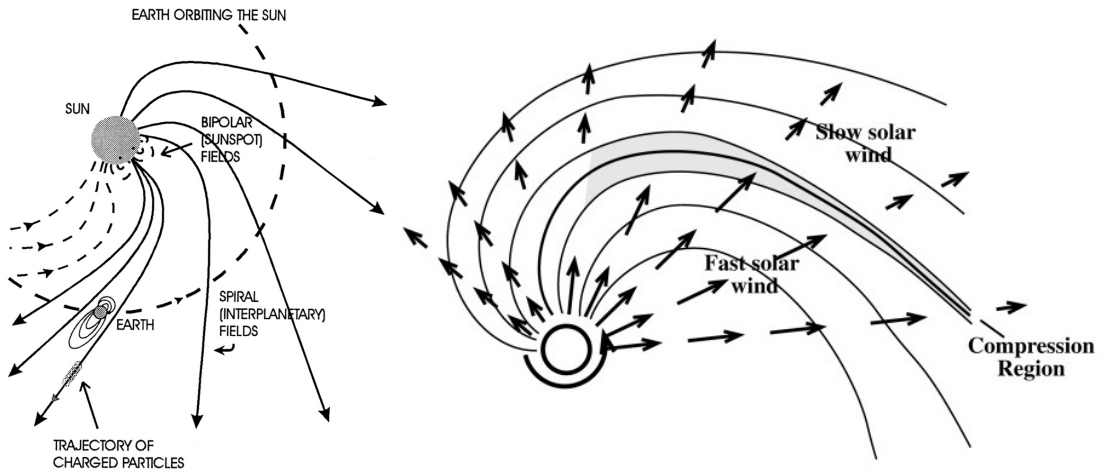

Figure 2.4: The left figure shows how the Sun's rotation causes the interplanetary field to take a spiral shape. Charged particles move along the field lines. The right figure shows how fast solar wind collides with slow solar wind causing compression regions of higher density and IMF disturbance. Credit: Vallée (1998) and Lyons (2003)

The amount of solar wind is connected with the solar activity. The number of sunspots, darker areas on the Sun's surface with large magnetic flux, is closely connected with solar activity. The solar maximum is defined as the time when the sunspot number is at its peak, and the solar minimum is when it is at its lowest. As sunspots have been documented for more than two centuries, a solar cycle has been established. This states that it takes about 11 years between two solar maximums (Bruevich & Bruevich, 2019). The Swarm satellites were launched in the 24th solar cycle, right before the solar maximum in 2014. The sunspot number for the duration of the Swarm mission shows that there is a maximum of about 150 sunspots during the first half of 2014, and then a steady decrease until a solar minimum in 2019/20 as seen in figure (2.5).

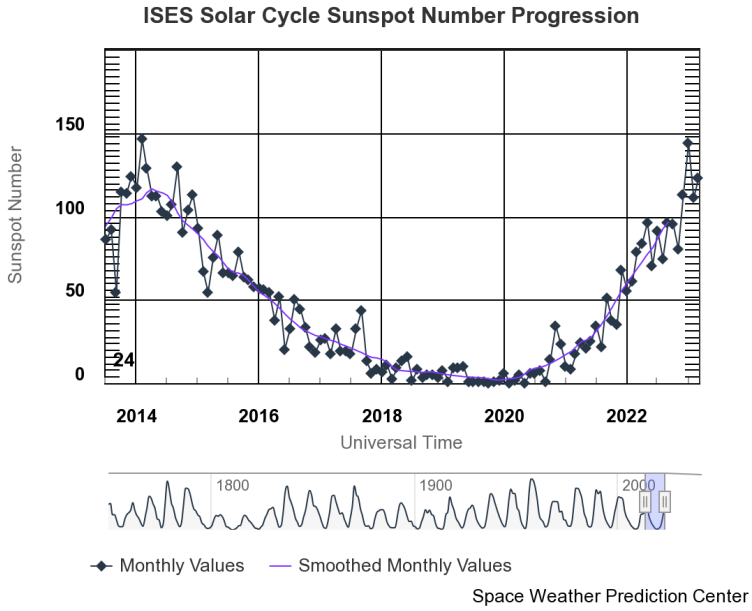

Figure 2.5: The number of sunspots between 2014 and 2023. The number 24 in the lower right corner represents the solar cycle number. The solar maximum of cycle 24 was in 2014, while it records a solar minimum around 2020. The smaller plot underneath shows all the recorded cycles with the time duration of the main plot marked in blue. Credit: NOAA https://www.swpc.noaa.gov/products/solar-cycle-progression

The Sun's corona, or outer atmosphere, is structured by strong magnetic fields. These fields can be both open and closed. Inside closed field lines vast amounts of energy in the form of plasma can be trapped. This energy can suddenly and violently be released, resulting in a massive amount of mass being accelerated to vast speeds into interplanetary space. This is an event called Coronal Mass Ejection, or CME (Garner, 2015). If a CME faces the Earth, the released plasma could result in a strong geomagnetic storm event on Earth (Russell et al., 2016).

2.3 Magnetosphere

The magnetosphere is a region around Earth that is influenced by the Earth's magnetic field produced mainly by the currents within the planet's molten interior. When the supersonic solar wind encounters the magnetosphere, it is slowed down, resulting in an increase in density and heat as more solar wind pushes from behind. This area is called the bow shock as the speed of the solar wind drastically reduces from supersonic to subsonic (Russell et al., 2016). The magnetosphere takes the shape of a teardrop, as a result of the the solar wind that flows toward and around it. When high-energy plasma in the solar wind hits the sunward side of the magnetosphere, the field lines will be compressed, while the antisunward side will be stretched out as it is dragged along by the passing solar wind. These two sides are often referred to as the dayside and nightside. The dayside of the magnetosphere usually reaches out to about 10 R_E (Earth radii), while the length of the nightside magnetosphere, or magnetotail, varies and is not well established. Still, it does extend well beyond the Moon's orbit at 60 R_E (McPherron, 1995; Prölss, 2010).

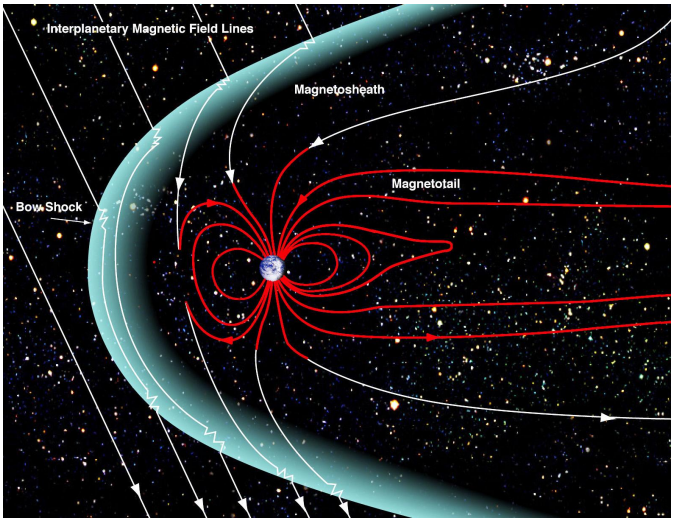

Figure 2.6: Figure of the magnetosphere showing the interplanetary magnetic field lines, the bow shock, the magnetosheath, and the magnetotail. Credit: NASA

The magnetosphere consists of closed and open field lines. A closed field line means that following a field line from the southern hemisphere will eventually lead back to the Earth's northern hemisphere, hence closing back on itself (See figure (2.6)). Open magnetic field lines are not actually open, but instead of closing back to Earth, like closed field lines, they close in interplanetary space, e.g. the Sun through the IMF. The boundary between the open and the closed magnetic field lines is called the open-closed boundary (OCB) and is located near the poles. As the Sun keeps spewing out material and IMF toward the Earth, the open field lines on the dayside get pushed toward the nightside and into the magnetotail. The closed field lines will be compressed, forcing the solar wind to flow around, thus acting as a shield for the Earth against the solar wind. This boundary between the solar wind and the Earth's magnetosphere is called the magnetopause (McPherron, 1995).

2.4 Earth's Ionosphere

In order to understand how the ionosphere is affected by a geomagnetic storm, it is important to have an underlying understanding of what the ionosphere is and the composition it is made up of. The ionosphere is part of the Earth's atmosphere where the gas has become partially or fully ionized (Gombosi, 1998; Russell et al., 2016). This ionization happens either by high-energy photons or high-energy particles hitting the neutral gas separating the electrons from the ions. Photons usually come from the sun, while ionizing particles can be interplanetary, come from the magnetosphere or from within the ionosphere itself, but mostly from the Sun (Russell et al., 2016). Even though this area of the atmosphere is called the ionosphere, the density of neutral is significantly higher than ions in most altitudes, as displayed in figure (2.7). Still, it is the ions that result in the different phenomena seen in the ionosphere (Kelley, 2009). The ionosphere is considered quasineutral, meaning that the number of positively charged ions and negatively charged electrons in a volume with a high number of charged particles is the same, giving a net charge of zero (Gombosi, 1998).

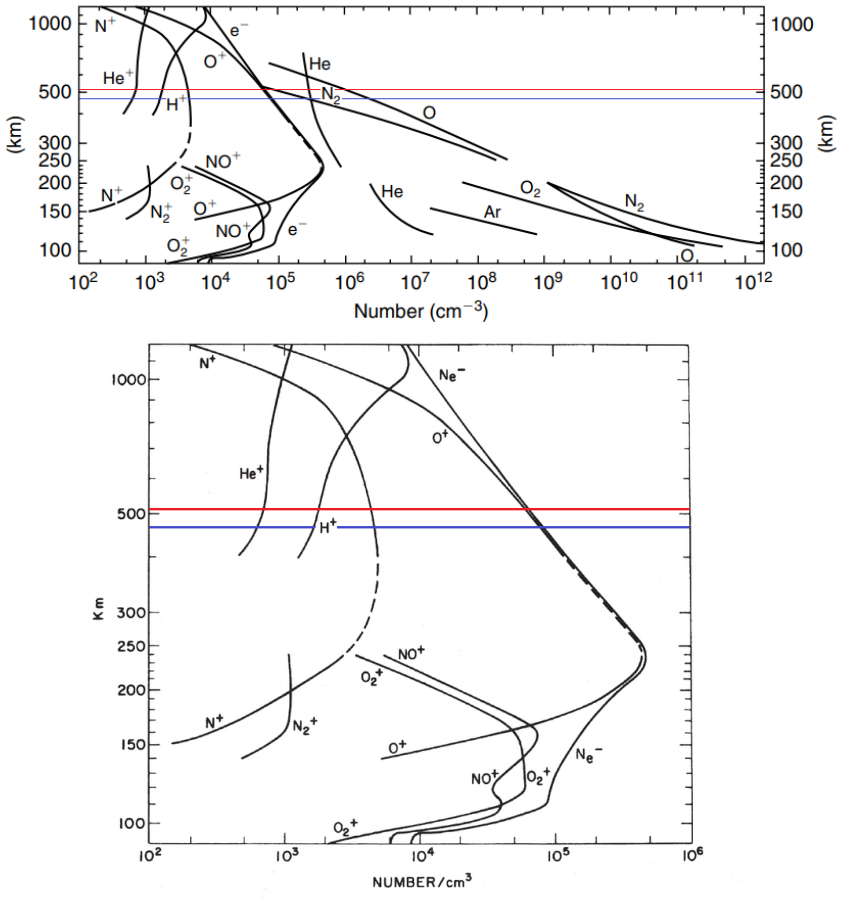

Figure 2.7: The composition of the ionosphere during daytime at mid-latitudes for low solar activity given in number density. The upper figure includes neutral composition, while the lower figure zooms in on the ion and electron densities. The ions are marked with a +-sign. The red line represents the altitude of Swarm B's orbit (510 km) while the blue represents Swarm A and C (460 km). Credit: (Kelley, 2009).

The ionosphere is divided into three regions; D, E, and F region. The F region is often divided into two subregions; F_1 and F_2 (Gombosi, 1998; Prölss, 2010). The region above the F_2 region is referred to as the topside ionosphere. The altitudes of the different regions may vary due to variations in solar activity but an approximate altitude and main ion composition can be seen in table (2.1). As the Swarm satellites orbit the Earth at an altitude of 460 km and 510 km, the main area of interest for this thesis will be the F region, particularly the F_2 with an altitude between 200-500 km and an ion composition consisting mainly of O^+. Studies have shown that the presence of lighter ions in the F-region altitudes is significant (Kelley, 2009; Smirnov et al., 2021). However, oxygen ions are the dominant species caused by the ionization of atomic oxygen, O, in this region (Gombosi, 1998). This reaction is as follows:

$$O + \gamma \rightarrow O^+ + e \tag{2.9}$$

where γ is the necessary energy for ionization to happen, and e is an electron. The ion production rate, S_i, in the region, is given by:

$$S_i = I_i n_O \tag{2.10}$$

where I_i is the photoionization coefficient of oxygen ($I_i \approx 10^{-7}\text{s}^{-1}$), and n_O is the oxygen density. The loss of oxygen ions involves a reaction with either nitrogen gas, N_2, or oxygen gas, O_2 (Gombosi, 1998). It is a two-step process with the first step being an atom-ion interchange:

$$O^+ + O_2 \rightarrow O_2^+ + O \qquad k_{O_2} \approx 2 \cdot 10^{-11}\ \text{cm}^3\text{s}^{-1} \tag{2.11}$$

$$O^+ + N_2 \rightarrow NO^+ + O \qquad k_{N_2} \approx 1 \cdot 10^{-12}\ \text{cm}^3\text{s}^{-1} \tag{2.12}$$

where k is the specific rate constant (a proportionality constant relating the rate of the reaction to the concentrations of reactants). These reactions are followed by a rapid recombination reaction where the newly produced molecular ions recombine with an electron, e:

$$O_2^+ + e \rightarrow O + O \qquad k_{O_2^+} \approx 3 \cdot 10^{-7}\ \text{cm}^3\text{s}^{-1} \tag{2.13}$$

$$NO^+ + e \rightarrow N + O \qquad k_{NO^+} \approx 3 \cdot 10^{-7}\ \text{cm}^3\text{s}^{-1} \tag{2.14}$$

The loss rate, L_i, can be calculated using only reaction (2.12) as the recombination process is faster with a factor of 10^4:

$$L_i n_e = n_e \left(k_{O_2} n_{O_2} + k_{N_2} n_{N_2}\right) \tag{2.15}$$

where n_e is the electron density. This gives the net production rate of ions, P_i, to be:

$$P_i = S_i - L_i n_e \tag{2.16}$$

From these reactions, it is clear that the amount of oxygen ions in the ionosphere depends on many different factors, most importantly the amount of solar radiation and the densities of neutrals necessary for the reactions to happen. Potential changes in the ionosphere neutral composition caused by a geomagnetic storm could therefore also change the ion composition.

Having described the basics of the ionosphere and magnetosphere, it is time to explain how they are connected to each other. This part is central to the thesis as the goal is to investigate the changes that happen to the effective ion mass in the ionosphere during a geomagnetic storm.

Region	Altitude (≈)	Main ion composition
D	60 - 90 km	NO^+, O_2^+, H_3O^+,
E	90 - 150 km	NO^+, O_2^+
F_1	150 - 200 km	O^+
F_2	200 - 500 km	O^+
Topside ionosphere	>500 km	O^+, H^+ , He^+

Table 2.1: The ionospheric regions with the approximate altitude and main ion composition (Gombosi, 1998; Kelley, 2009; Prölss, 2010).

2.5 Magnetosphere-Ionosphere Coupling

The increase in energy in the ionosphere during a geomagnetic storm is directly related to the couplings between the ionosphere and the magnetosphere (Russell et al., 2016). The solar wind's interaction with the magnetosphere sets up different currents both in the magnetosphere and ionosphere making it possible for energy to be transported between them. Before showing the different currents, an explanation of the solar wind interaction with the magnetosphere, the Dungey cycle, will be presented.

Magnetic reconnection can happen either at the dayside of the magnetosphere or in the magnetotail. The Earth's magnetic field is northward at the equatorial dayside, ergo the IMF must have a southward B_z component in order to be antiparallel. The solar wind flow acts as an external flow that pushes the antiparallel magnetic field lines toward each other, resulting in reconnection. On the other side, the magnetotail, the Earth's open field lines are already antiparallel to each other. But in order for reconnection to happen there must be an external force pushing them towards each other. As the solar wind passes around the magnetopause, a magnetic flux happens as the open field lines move with the solar wind into the tail. The increase of magnetic field lines in the tail creates the necessary force making magnetic reconnection possible. When nightside reconnection takes place, a massive amount of charged particles that have been stored in the tail will be flung, along the newly closed field line, toward the Earth's poles (Russell et al., 2016). In the tail, reconnection is not dependent on the IMF having a southward component (Priest & Forbes, 2000).

The Dungey cycle is the process that starts when a closed field line on the dayside reconnects with the IMF (Dungey, 1961). As shown in figure (2.8), the numbers 1-9 represent the different steps that happen during the Dungey cycle. Firstly, the IMF that is frozen-in to the solar wind must be southward. It takes a slightly bent shape as the plasma in the solar wind hits the bow shock at different times. Number 1 represents a closed field line right at the inside of the magnetopause and 1' represents the IMF line right outside of the magnetopause. As explained above, reconnection between the two antiparallel field lines occur, and the closed field line becomes an open field line. The open field line moves with the solar wind into the tail, represented by 2-5 in figure (2.8). The increase of magnetic field lines forces the two antiparallel open field lines, 6 and 6', closer together until they break apart into a closed magnetic field line connected to Earth, 7, and an IMF line, 7'. Lastly, the newly closed magnetic field line will travel sunward along the Earth's side and concludes the cycle when it is back at the dayside, shown in number 9 (Russell et al., 2016).

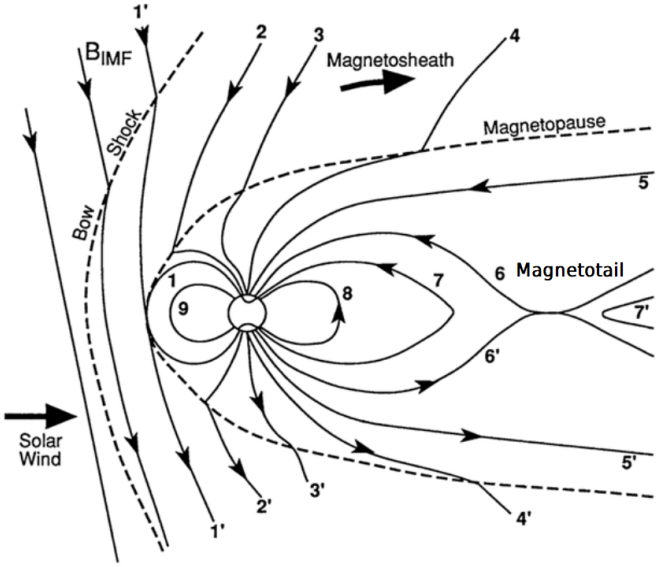

Figure 2.8: Regions of the Earth's magnetosphere and example of the Dungey cycle. Credit: Russell et al. (2016)

.

The Dungey cycle sets up several different currents in the magnetosphere and ionosphere. An example of the current systems can be seen in figure (2.9). In this thesis, the ring current and the field-aligned currents (FAC) are central. The ring current is closely connected with the strength and density of the solar wind. The field-aligned currents, i.e. Birkeland currents (region 1 and region 2 currents), are currents that move along the magnetic field lines traversing both the ionosphere and magnetosphere (McPherron, 1995). The movement of charges through both regions results in increased temperature, ionization, and density in the affected areas.

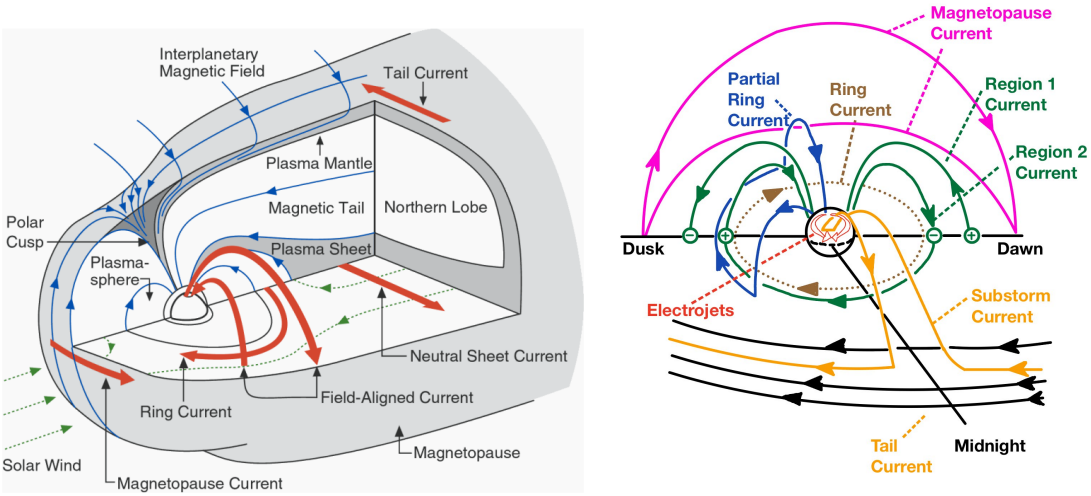

Figure 2.9: Current systems in the magnetosphere and ionosphere. The field-aligned currents (FAC) are central to the coupling between the ionosphere and magnetosphere. Credit: Nakariakov et al. (2016) and McPherron (1995)

2.6 Geomagnetic Storms

A geomagnetic storm is a phenomenon that takes place during prolonged dayside reconnection due to a coronal mass ejection (CME) or another high-energy event at the Sun. A vast amount of energy gets exchanged from the solar wind into the magnetosphere and ionosphere, resulting in currents, temperature, and composition changes. In the magnetotail, there will be an increase in high-energy plasma. A large number of particles will increase the ring current, as the high energy particles will get trapped in the outer closed field lines in the magnetosphere (McPherron, 1995; Prölss, 2010; Russell et al., 2016). A geomagnetic storm usually lasts for several days and moves through different phases. These phases are easily spotted by the Dst-index, which will be explained in section (2.7). When the solar wind first hits the Earth's magnetosphere, it will lead to a compression of the magnetic field lines. This compression can be measured by magnetometers on the Earth's surface and will show a sudden jump in the horizontal component of the magnetic field. This is called the Storm Sudden Commencement (SSC) (Russell et al., 2016). Later, the increase of the ring current will result in a significant decrease in the same magnetic field component as seen in figure (2.10). The duration where the ring current increases is called the storm's main phase. The storm enters its recovery phase when the IMF turns northward again, reconnection ends, and the ring current stops growing. Over the next few days, the ring current will gradually return to pre-storm values, and the storm is history (Cander & Mihajlovic, 1998; Prölss, 2010).

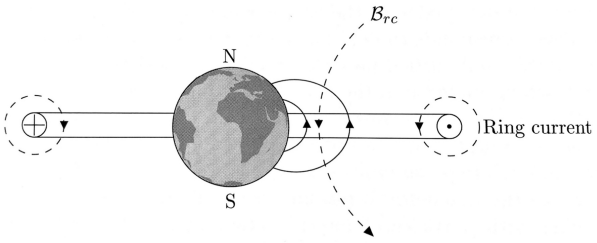

Figure 2.10: Visualization of how the ring current disturbs the Earth's magnetic field. These disturbances are measured and used as an indication of an ongoing geomagnetic storm. Credit: Prölss (2010)

2.7 Storm indices

Dst-index

The magnetic disturbance in the horizontal component of Earth's magnetic field, caused by the increase of the storm time ring current, is measured by the Disturbance storm time - index (Dst-index) (Mayaud, 1980; Russell et al., 2016; Sugiura, 1991). This index is considered one of the most accurate of the geomagnetic indices, as it monitors the phenomena in which it was designed with great accuracy (Mayaud, 1980). As the ring current flows in the equatorial magnetosphere, four stations positioned at lower latitudes are used to measure the disturbances created by the solar wind's interaction with the magnetosphere. This is done by creating a baseline of the average minimum ring current and the background magnetic field during quiet days and removing this from the recorded measurements (Russell et al., 2016). The result is a characteristic plot of disturbances that makes it easy to identify the SSC, the main phase, and the recovery phase of a

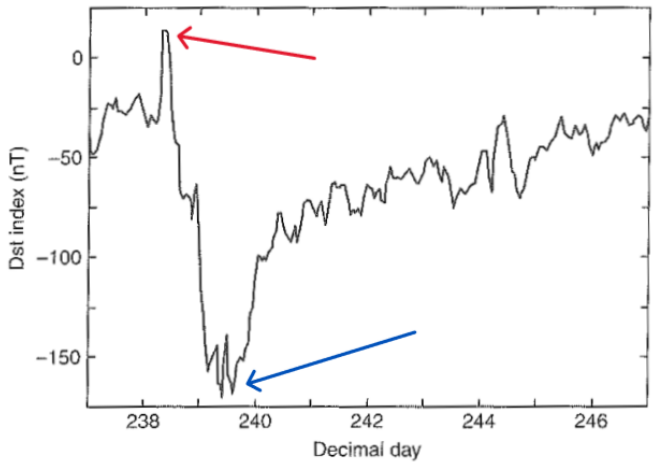

Figure 2.11: A typical example of a geomagnetic storm observed in the Dst-index. The red arrow shows the storm sudden commencement (SSC) with a rapid increase in the magnetic field strength. The storm results in an increase in the ring current, which in turn induces a horizontal magnetic field that is recorded as a significant drop in Dst until the Dst-minimum, marked with the blue arrow. The time period between the SSC and Dst-minimum is considered the storm's main phase. The ring current decays over the next week, denoting the recovery phase of the storm.

storm. An example of a typical storm as seen by the Dst-index is given in figure (2.11). Here it is possible to spot a sudden increase in the horizontal magnetic field indicating a SSC (marked by the red arrow in figure (2.11)). This is followed by a significant drop in Dst marking the Dst-minimum (blue arrow), before the storm enters into its recovery phase where the disturbance slowly decreases. The records of the Dst-index are provided by the World Data Center for Geomagnetism in Kyoto, Japan, and can be accessed from their web page: https://wdc.kugi.kyoto-u.ac.jp/index.html

K_p-index

The K_p-index is a measure of the global geomagnetic activity level, with higher values indicating more intense geomagnetic storms. The index can be represented in different ways but in this thesis the symbol notation by $K_p = 0o, 0+, 1-, 1o, 1+, \ldots, 9-, 9$, where o, +, and −represent the integer (o), plus one third (+) and minus one third (−), is used (Jordan, 2023; Matzka et al., 2021). The K_p-index is derived from the maximum fluctuations in the horizontal component of the Earth's magnetic field observed at a set of standard observatories located around the world (Matzka et al., 2021). In this project, it is mainly used as a tool for identifying possible storms to study.

2.8 Energy transport

A geomagnetic storm is an event of enhanced dissipation of energy from the solar wind into the near-Earth space environment that can reach dissipation rates up to 10^{12} W (Prölss, 2010). All regions of the space environment are affected, even the lower latitudes of the ionosphere, implying that it is a global event. It is not possible to fully explain all the different aspects of how a geomagnetic storm affects the Earth in a single thesis. Therefore the main focus of this thesis will be on the changes happening to the equatorial region of the ionosphere as this is where the SLIDEM data of the effective ion mass is available.

Significant parts of the solar wind energy are absorbed by the polar upper atmosphere through the current systems. The absorbed energy can lead to heating so intense that it produces disturbances not only in the polar regions but globally. There are several ways of explaining how the disturbance propagates to different parts of the Earth, but especially one phenomenon leads to significant density disturbances in the equatorial regions. This phenomenon is called traveling atmospheric disturbance (TAD). It is understood to be *"an impulse-like disturbance arising from a superposition of atmospheric gravity waves that propagate at high velocity (500 - 1000 m/s) from polar to equatorial regions"* (Prölss, 2010, p.427). Gravity waves are defined as a wave moving through a stable layer of the atmosphere, much like ripples in a pond but with air (NOAA, 2021). During a storm (or substorm), the energy dispatched to the polar regions (marked as a pink wave in figure (2.12)) leads to an expansion of gases, and an increase in temperature and density causing several TADs to propagate outwards covering all of Earth. When TADs (shown as blue waves in figure(2.12)) originating from opposite poles meet each other at the equatorial region, a superposition of the disturbances leads to an increase in the density and temperature of the equatorial ionosphere (shown in red in figure (2.12)). In turn, this will cause a vertical expansion of the ionosphere (Prölss, 2010). As the ionosphere expands upwards, the net ion production will increase along with it. This is due to the density of molecular nitrogen and oxygen, responsible for the loss of ionization, decreasing faster with altitude than atomic oxygen, which governs the ion production rate. Consequently, both the height and the value of the maximum ionization density will increase (Prölss, 2010). From the velocity of the TADs, one can calculate the time it takes for them to reach the equator. This is estimated to take around four hours from the storm's onset (figure (2.12)).

This chapter's goal has been to present the theoretical foundation for the thesis, as it is important in order to understand the observed changes to the ionosphere's ion composition. The thesis will now continue with an introduction of the data and methodology used in this project before the observations are presented and discussed.

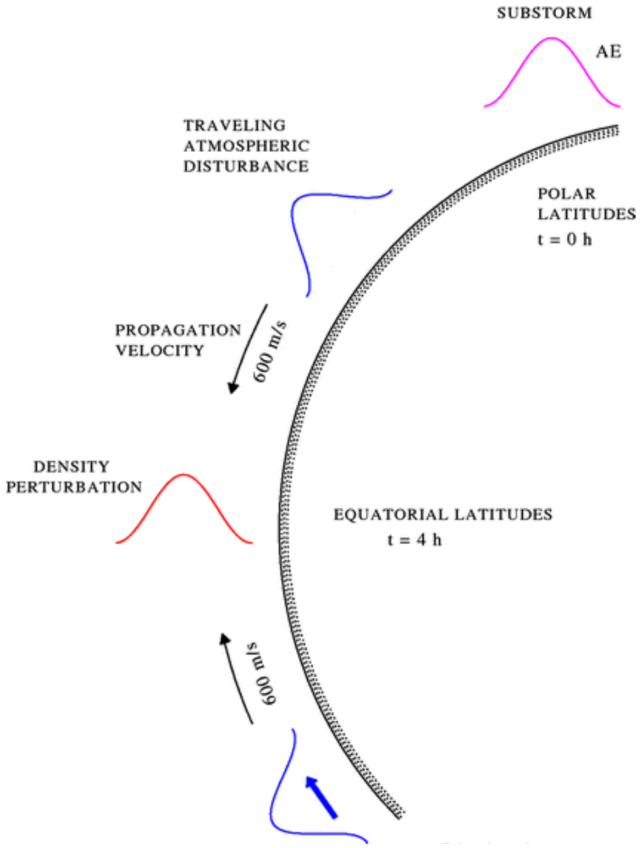

Figure 2.12: The propagation of traveling atmospheric disturbance (TAD) originating from (sub)storm activity at the poles results in density perturbation at the equatorial region. The time indications imply the time it takes for the TAD to reach equatorial latitudes after the onset of the storm event. Credit: Prölss (2010)

Chapter 3

Data and Methods

The source of data that has been used in this project is the OMNI data, used to collect solar wind data, and the data produced by the SLIDEM product from data collected by the Swarm satellites. The data have been collected from the European Space Agency's (ESA) website. This chapter will present this data and the usage of it.

3.1 Swarm

The Swarm mission is a mission within the European Space Agency's Earth Explorer Program. The mission's aim is to measure the Earth's magnetic field with unprecedented accuracy (Battrick, B., 2004; Friis-Christensen et al., 2008). To achieve this, three identical satellites, Swarm A, B, and C, were launched into near-polar orbit in late 2013 (Wood et al., 2022). Swarm A and C orbit side by side with a 1.5° longitudinal separation at an altitude of 460 km, while Swarm B orbits at an altitude of 510 km. As a result of the difference in altitude, Swarm B's orbit slowly drifts away from that of Swarm A and C (Friis-Christensen et al., 2008). The satellites carry several instruments on board as seen in figure (3.1). For this project, the Electric Field Instruments, Langmuir Probes, Thermal Ion Imager(TII), the faceplate, and the satellite's GPS system are used (Pakhotin et al., 2022).

3.2 SLIDEM Data

The Swarm Langmuir Probe Ion drift, Density, and Effective Mass (SLIDEM) product was developed to relax some of the assumptions inherent in current ESA Swarm density estimates (Pakhotin et al., 2022). Swarm ion densities are typically estimated from the ion admittance, d_i, (derivative of current with respect to applied voltage) and is given by:

$$d_i = \frac{\partial I}{\partial V_b} = -\frac{2N_i q_i^2 \pi r_p^2}{m_i v_i} \tag{3.1}$$

where I is the current in the probe, V_b is the Langmuir probe bias, N_i is the ion density, q_i is the ion charge, r_p is the Langmuir probe radius, m_i is the ion mass, and v_i is the along-track component of ion drift.

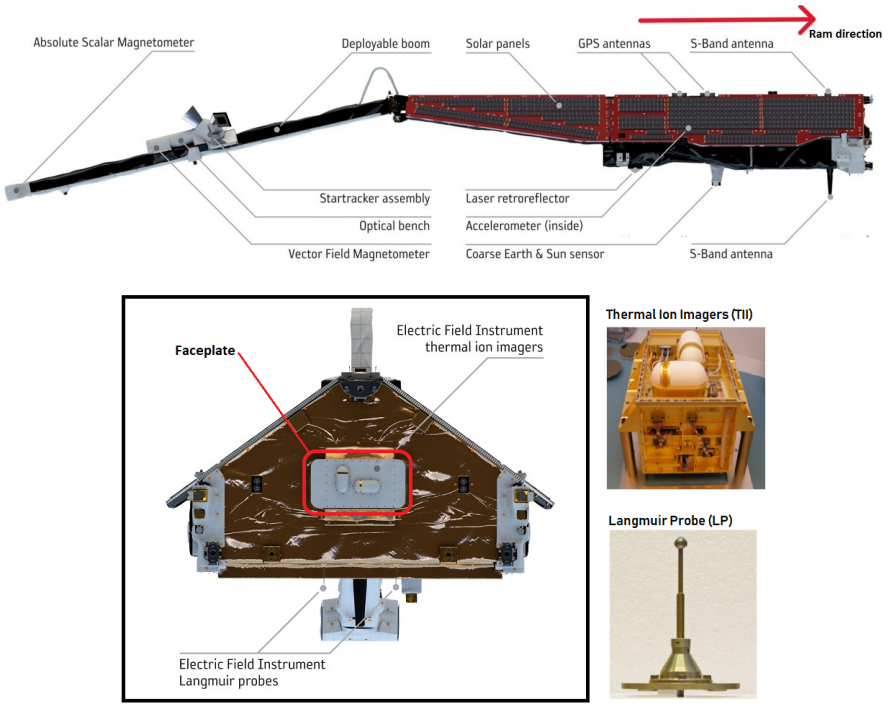

Figure 3.1: The Swarm Spacecraft instruments. The red arrow on the upper picture shows the satellite's traveling direction (Ram direction). In the lower left picture, the faceplate is marked in red. Image credit: The European Space Agency.

An issue in calculating density in this matter is that two necessary assumptions have been made. Firstly, the surrounding plasma consists only of single-charged oxygen ions. This is not always the case (Smirnov et al., 2021). Secondly, that v_s is equal to the satellite speed. In the polar regions, it is already shown in the theory section that strong ion drifts can occur. Hence these assumptions are expected to be violated.

By neglecting the interference by the plasma sheath (charged sheath that could affect the effective area of the Langmuir probe), assuming ions traveling at equal speed, v_i, and having a single charge, e, and mass is replaced by effective mass, M_{eff}, the expression becomes :

$$d_i = -\frac{2N_i e^2 \pi r_p^2}{M_{eff} v_i} \tag{3.2}$$

where

$$N_i = \sum_{s=1}^{Species} N_s \tag{3.3}$$

and

$$\frac{1}{M_{eff}} = \frac{1}{N_i} \sum_{s=1}^{S} N_s \frac{1}{m_s} \tag{3.4}$$

where N_s and m_s are the density and mass of the different ion species. It is important to note that M_{eff}, also called reduced mass, is much more sensitive to small percentages of lighter ions than average mass. For instance, a change from 0 % H^+ to a 5 % H^+ in the ion composition will reduce the value from 16 u to 9.1 u (Pakhotin et al., 2022).

Furthermore, the SLIDEM product produces an estimate of the ion density believed to be more precise as it introduces the TII faceplate current measurements (Burchill et al., 2022; Pakhotin et al., 2022). This current, with the same assumptions as above, is given as

$$I_{FP} = -N_i e v_i A_{FP} \tag{3.5}$$

where A_{FP} is the faceplate area (see figure 3.1). This can then be combined with equation (3.1) to get a new equation for ion density and along-track ion drift:

$$N_i = \sqrt{\frac{-d_i I_{FP} M_{eff}}{2e^3 A_{FP} \pi r_p^2}} \tag{3.6}$$

and

$$v_i = v_{sat} - \sqrt{\frac{-2e\pi r_p^2 I_{FP}}{d_i A_{FP} M_{eff}}} \tag{3.7}$$

From these equations, assuming that the along-track ion drift can be neglected in latitudes between +/- 50 degrees, they get an expression for the effective ion mass:

$$M_{eff} = \frac{2e\pi r_p^2 I_{FP}}{d_i A_{FP} v_{sat}^2} \tag{3.8}$$

As the faceplate is negatively charged, ions will be pulled towards it, resulting in more ions hitting the faceplate than the area suggests. Similarly, the Langmuir probes are positioned near the negatively charged satellite body, subsequently affecting the number of ions hitting it. Resendiz Lira et al. (2019) and Resendiz Lira and Marchand (2021) showed it is necessary with a correction factor for both these areas. Adding these corrections to the effective ion mass equation gives us

$$M_{eff} = \frac{2e(1-\delta_{LP})\pi r_p^2 I_{FP}}{d_i(1+\delta_{FP}) A_{FP} v_{sat}^2} \tag{3.9}$$

where δ_{LP} and δ_{FP} are the correction term for the effective Langmuir probe and faceplate area.

This equation (3.9) makes up the foundation of the data used in this thesis. A data processor at ESA gathers the necessary input data from Swarm and generates the SLIDEM data using the presented equations. This is downloadable from their website (ESA, 2023).

An important matter is that the faceplate bias can be set between -1 to -5 V. To optimize the TII operations it is often set to -1 V (Knudsen et al., 2017). This could however contaminate the ion current as this voltage does not sufficiently repel electrons (Pakhotin et al., 2022). To get reliable ion density estimates, the bias is set to -3.5 V. As a result of this, the SLIDEM product data is only available during the lower faceplate voltage.

3.3 OMNI data

Solar wind data is important for understanding space weather. For the sake of this project, the data used is the "OMNI_HRO_1min" downloaded from NASA's website (King and Papitashvili, 2008). The data includes solar wind parameters provided by the ACE and WIND satellites. Since the satellites orbit the gravitational equilibrium between the Earth and the Sun, the data collected have been time-shifted in order to make the data easily comparable. Additionally, the SYM/H-index (Dst-index) is integrated into the data set providing an easy option of getting the necessary space weather parameters from the same website.

3.4 Storm Identification

The first part of the project was to decide which geomagnetic storms should be analyzed. The Swarm satellites have been in operation since 2014 (Wood et al., 2022), so the storms must have happened between then and today. Choosing the five largest storms depending on the Dst-index, was a thought that quickly came to mind. Going through the Dst-index for each month since 2014, and comparing those with an overview of the largest recorded storms (Parsec, 2023) and the K_p-index (GFZ, 2023), five storms with a minimum Dst-value of about 150 nT or lower was chosen. See table (3.1) for the selected storms.

The chosen amount of data was based on the time of the minimum Dst-value and then +/- 5 days. Gathering the data was done with a small snippet of code. As the data downloaded from the ESA's website is given in the CDF format (Common Data File), a code was written to extract the data from each day and save it as a binary file, one for each satellite, three for each storm.

SLIDEM has several time gaps in the produced data set. The voltage of the faceplate bias is a potential reason for this (Pakhotin et al., 2022). For some of the storms, data is absent for about one day around the time when the Dst was at its minimum. Still, there is enough data to reveal useful observations. However, several days of data were lacking for the selected March 2015 storm. The storm was thus discarded for not having adequate data on the effective ion mass.

Storm	Time of minimum dst	Dst-value [nT]	K_p-value
March 2015	17-03-2015 23:50	-234	8-
June 2015	23-06-2015 04:24	-208	8+
December 2015	20-12-2015 22:49	-170	7
September 2017	08-09-2017 01:08	-146	8+
August 2018	26-08-2018 07:11	-206	7+

Table 3.1: Table of the selected storms and value of indices. March 2015 was later discarded as not enough data was available.

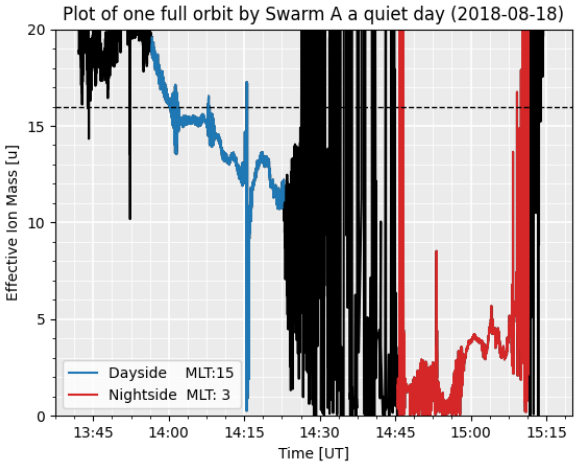

(a)

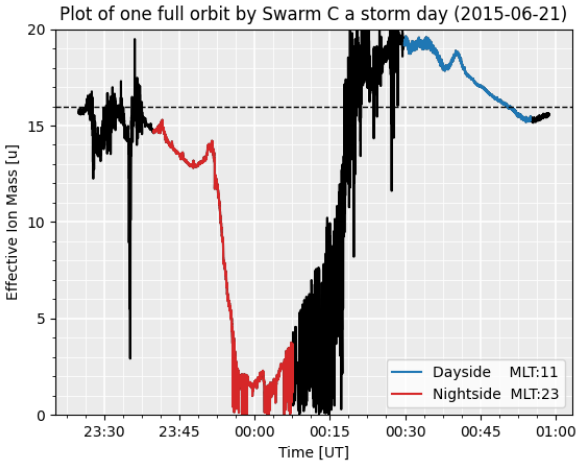

(b)

Figure 3.2: Two examples of complete orbits. (a) complete orbit of Swarm A on a randomly picked date, (b) complete orbit of Swarm C a day during the June 2015 storm. The black areas of the graph represent the data that are outside the valid perimeters of +/- 50 QDLat. The blue graphs are the valid M_{eff} data on the nightside and, similarly, the red represents the dayside. Oxygen ions are used as a reference, represented by the black, horizontal line.

3.5 Analyzing SLIDEM data

The SLIDEM product downloaded from the ESA includes daily data of several different parameters as shown in table (3.2). For this thesis, the data used is the Timestamp, Magnetic Local Time data (MLT), Latitude, Quasi Dipole Latitude (QDLat), Ion Effective Mass, Mass Uncertainty, Validity Flags, and the TBT-2015 topside ion composition model (IRI-2016).

As the SLIDEM product is only considered reliable for values of the effective ion mass when there is no significant along-track ion drift, the data has to be analyzed to avoid this. As the product description explains, Swarm satellites are assumed to have

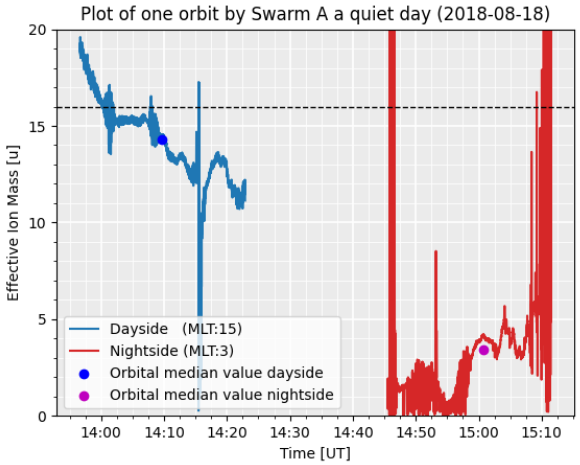

(a)

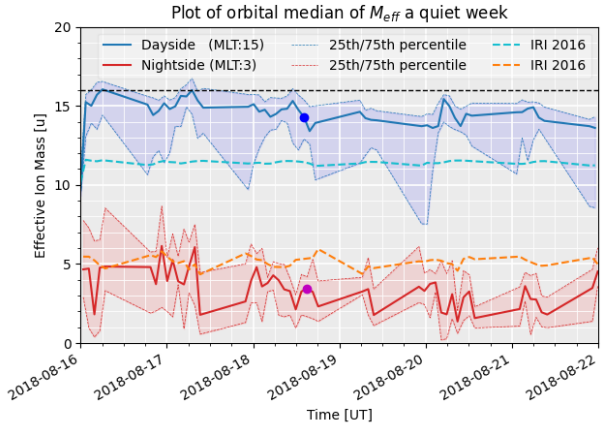

(b)

Figure 3.3: Figure (a) shows the valid, data produced by the SLIDEM product of the effective ion mass during a single orbit of Swarm A. The horizontal black line is the mass of an oxygen ion, 16 u. The pink and blue dots represent the median value of effective mass for the orbit divided into dayside and nightside. Figure (b) shows how the median effective mass for every orbit is plotted for a quiet week. The blue graph shows the dayside median with the 25th and 75th percentile as the upper and lower boundary. Similarly, the red graph shows this for the nightside. The red and blue dots are the same as in Figure (a). The dashed graphs show the IRI-2016 values of the effective mass during the day (cyan) and night (orange).

no significant along-track ion drift when in between a QDLatitude of +/- 50 degrees (Burchill et al., 2022). The product's data set does include values on the effective mass even at higher latitudes. Figure (3.2) shows an example of all data gathered during one full orbit on a quiet day (3.2a) and a storm day (3.2b). The blue areas of the graph show the valid dayside values, while the red areas show the valid nightside values. The black areas of the graphs in figure (3.2) have large fluctuations, which shows that data outside of these boundaries are unreliable. However, fluctuations are visible in the valid data as well, especially at the nightside. The SLIDEM product has a default value of -1 for the M_{eff} if the product is somehow unable to calculate the effective mass. All these data points were filtered out early in the analysis process. As the data will vary depending

on the satellite's latitude, and includes deviating data points, it became obvious that sampling the data would be crucial to get readable and comparable results. The data was flagged with an "Orbit Number", enabling the possibility of averaging the collected data into the different orbits traversed by the satellites. This was done by defining an orbit as when the satellite crossed the 70° Latitude line traveling northward as the beginning of the next orbit and the end of the previous one. Checking two consecutive elements of Latitude where the second is larger than 70° and the first is smaller than 70°, is a simple solution for this. Consequently applying the orbit number as a flag. An example of a plot of one single orbit is given in figure (3.3a), which shows the same as figure (3.2a) but now excluding values outside the QDLatitude range. The red graph marks the dayside values and the blue the nightside values. Extracting a median value from the orbit data is done to get a good basis for comparison, shown as a red and blue dot in figure (3.3a). The median value is used instead of an average since the data set often includes some data points that would contaminate the average value. Plotting the orbital median would then give a more clear picture of what is happening over time. An example is shown in figure (3.3b) where the orbital median for a quiet week is plotted together with the 25th/75th percentiles. The blue graph shows that the dayside median values are between 14-16 u and the red graph shows a median value between 1-5 u. The dashed cyan and orange lines represent the International Reference Ionosphere 2016 (IRI-2016) values corresponding to the period. IRI-2016 is a standardized empirical model used to describe the ionosphere and topside ionosphere. It incorporates reliable data sources to determine key parameters, such as electron density, ion composition, electron temperature, ion temperature, and more, over an altitude range of 60 to 2000 km (Truhlik et al., 2015). Since the SLIDEM product is thought to capture the composition changes better than the IRI-2016 (Pakhotin et al., 2022), in this thesis it is only used as a comparison for the quiet week baseline observations (figure (3.3b)).

3.6 Implementing the OMNI data

For this thesis, it is important with an understanding of what is going on in space during the respective storms being investigated. By downloading the OMNI data for the same duration as the storms, it can be used to better understand what happens during a storm. Here, data on the magnitude of the IMF, the z-component of the IMF, flow pressure, and Dst-index were gathered and plotted as shown in the results. As the data had already been time shifted to Earth's time, the only adjustment needed to be done before plotting was to mask the data points where default values had been used. A small code snippet was used for these adjustments, and the rest of the data was plotted.

Variable	Unit	Note
Timestamp	ms	UTC
Latitude	deg	Geodetic latitude
Longitude	deg	Geodetic longitude
Radius	m	Geocentric radius
Height	m	Height above WGS84 reference ellipsoid
QDLatitude	deg	Quasi-dipole magnetic latitude
MLT	hour	Magnetic local time
V_sat_nec	m/s	Sat velocity in north, east, centre reference frame
M_i_eff	u	Ion effective mass
M_i_eff_err	u	Ion effective mass uncertainty
M_i_rff_Flags		Ion effective mass validity flag
M_i_eff_tbt_model	u	Ion effective mass model (IRI-2016)
V_i	m/s	Along-track component of ion drift velocity
V_i_err	m/s	Ion drift velocity resolution estimate
V_i_Flags		Ion drift velocity validity flag
V_i_raw	m/s	Uncorrected ion drift velocity
N_i	cm^3	Revised estimate of ion density
N_i_err	cm^3	Ion density uncertainty
N_i_Flags		Ion density validity flag
A_fp	m^2	Modified-OML faceplate area
R_p	m	Modified-OML Langmuir probe radius
T_e	K	Electron temperature used in modified OML
Phi_sc	V	Satellite potential used in modified OML

Table 3.2: Table with an overview of the different variables included in the SLIDEM product (Burchill et al., 2022).

Chapter 4

Observations

In this chapter, the relevant observations done throughout the project will be displayed and commented on. The chapter is divided into five sections, one short section on the baseline values and one section for each of the storms. Every storm will have a plot of the solar wind data gathered from OMNI, plots showing the effective ion mass, and comments regarding the plots. All plots are time series and run approximately from three days prior to the Dst-minimum to three days after.

4.1 Baseline values

When analyzing the data produced during a storm a baseline value is necessary for comparison. For this reason, approximately one week of data prior to each storm was used to establish an average baseline value of the effective ion mass. This is shown in table (4.1). The table includes a row for each storm, split into columns for the three different satellites which again is divided into dayside and nightside values. It shows that there is a baseline offset between the different storms. Swarm A and C have similar baseline values during each storm with only minor differences ($\lesssim 1$ u). The exception is the nightside of the August 18 storm where the difference is 2.5 u. Swarm B shows similar baseline values as A and C on the dayside but is significantly below the two others on the nightside. In general, the dayside baseline is showing higher values on the dayside than the nightside. The June 15 storm has the highest values at the dayside while it decreases with ≈ 1 u prior to the December 15 storm, and another ≈ 2 u each for the last two storms. The nightside values vary more, with the highest values before the December 15 storm, and the lowest values before the August 18 storm. With the

Storm	**Swarm A**		**Swarm B**		**Swarm C**	
	Day	**Night**	**Day**	**Night**	**Day**	**Night**
June 15	19.09	15.30	18.88	11.21	18.08	14.40
December 15	18.17	17.30	17.66	13.10	17.45	16.01
September 17	16.10	11.31	15.05	4.18	15.61	11.08
August 18	14.05	4.68	6.38	2.99	13.73	7.09

Table 4.1: Table with baseline values of M_{eff} by calculating the average value based on the SLIDEM data one week prior to the storms. All numbers are given in u.

baseline values established, it is time to present the SLIDEM product's data on the effective ion mass during four different geomagnetic storms starting with the June 2015 storm.

4.2 June 2015 Storm

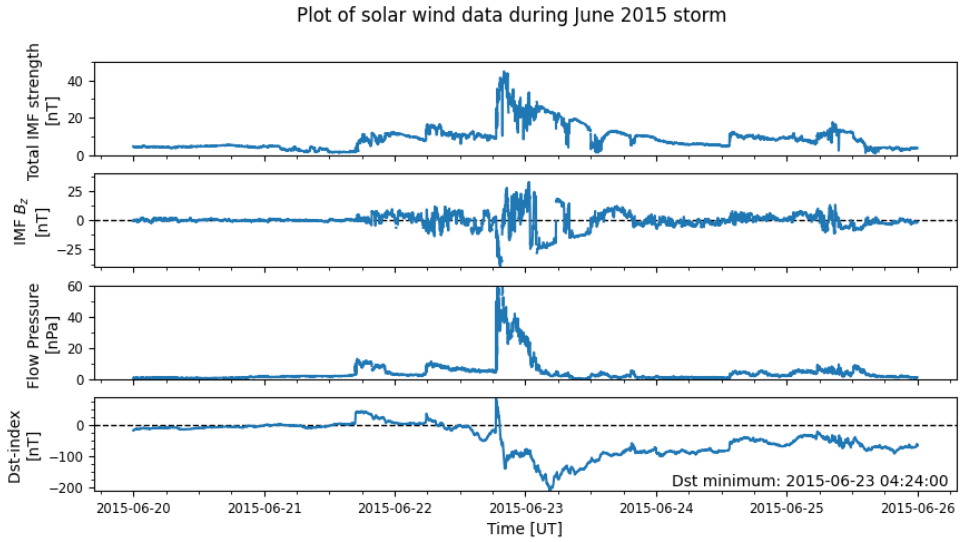

Figure 4.1: Solar wind data during the June 2015 storm. The first plot shows the magnitude of the IMF. The second shows the z-component of the IMF. The third shows the flow pressure. Lastly, the Dst-index is plotted. The bottom right corner shows the timestamp for when the Dst-index is at its lowest.

Figure (4.1) consists of four plots. They are time series and share an x-axis to make them easily comparable with each other. The first plot shows the total IMF strength measured in nT. B_z contributes to the total IMF strength, but as it is an important factor of solar wind's impact on the Earth, it is plotted separately in the second plot. Thirdly, the flow pressure of the solar wind is plotted. This is a parameter OMNI derives from the proton density, N_p, given in cm^{-3}, and the proton velocity, v_p, in km/s. The unit is nPa, which expresses the dynamic force the solar wind applies to the magnetosphere. Lastly, the Dst-index given in nT is plotted. This last data is strictly speaking not solar wind data, but it is provided by OMNI through WDC Kyoto as it is an important indicator of how the solar wind influences the Earth.

The solar wind data (4.1) shows activity starting in the evening of the 21st. The IMF strength reaches its maximum about 24 hours later. The z-component of the IMF fluctuates, but a significant drop can be observed simultaneously with the increase in field strength. There is also a significant increase in the flow pressure. The solar wind activities impact the Dst-index, and the storm's main phase can be observed beginning around 18:00 on the 22nd lasting until the Dst-minimum some hours later. After this, the recovery phase can be seen as the Dst value slowly increases and the solar wind calms down.

Figure (4.2) is the orbital median of the effective ion mass produced from the SLIDEM data set. The figure is split into two plots, one for the dayside and one for nightside. The vertical dashed line shows the time of the storm's minimum Dst, and the horizontal dashed line represents the mass of an oxygen ion, 16 u. A 24-hour data gap can be observed on the 23rd, which includes the time when the storm reaches its lowest Dst value. All three satellites have orbits that are almost midday-midnight with MLT of 11

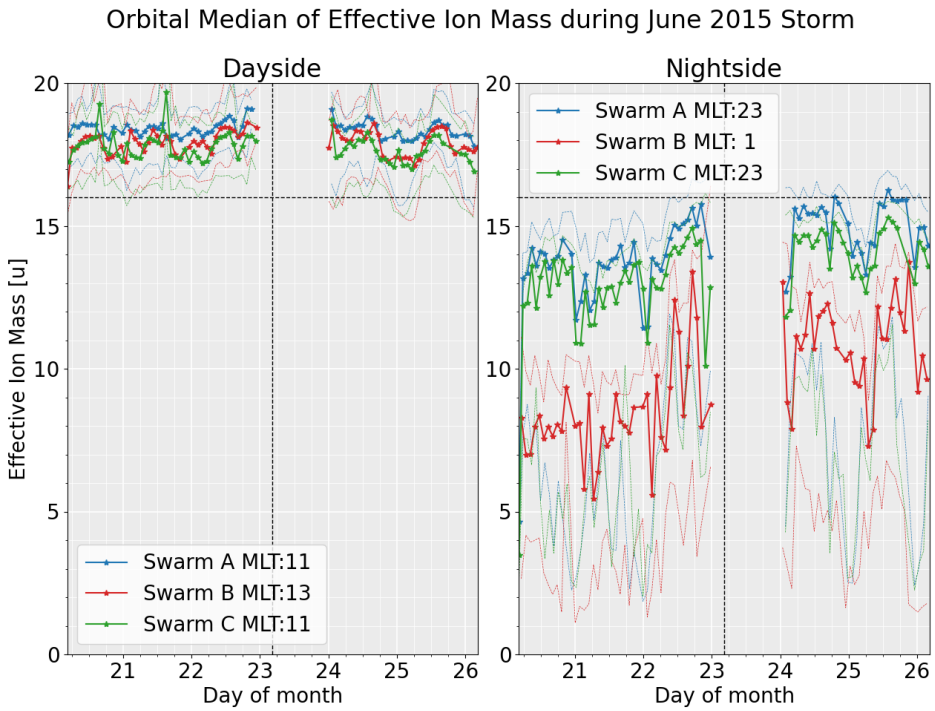

Figure 4.2: The orbital median of the Effective Ion Mass for the June 2015 storm. The figure contains one plot with dayside values and one for nightside. The dashed colored lines represent the 25/75 percentile of the M_{eff}. Time, expressed in the day of the month, is shown on the x-axis, and effective ion mass on the y-axis. The vertical dotted line shows the time of the storm's Dst-minimum, and the dotted horizontal line equals the mass of an oxygen ion, 16 u.

to 23 (Swarm A and C) and 13 to 01 (Swarm B). At the dayside, all satellites display values well above the 16 u line. During the first couple of days, effective mass stays mostly between 17-19 u, with Swarm A generally showing a slightly higher value than the two other satellites. About half a day prior to the minimum Dst an increase may be observed reaching its maximum value as it reaches the data gap. Swarm B measures a significantly lower value of the effective mass at the nightside than what the other satellites do.

4.3 December 2015 Storm

The development of the second storm is seen in the figure of the solar wind data (4.3). The plot has the same format as figure (4.1), hence the structure will not be commented on in this or the following storms. The data shows how the solar wind has a significant increase in IMF strength and flow pressure on the evening of the 19th. B_z at this time is fluctuating quickly between positive and negative values and a positive increase in the Dst-index is observed. In the early morning hours of the 20th, the IMF switches southward for a prolonged amount of time. Here, the Dst drops and the storm enters its main phase. It reaches its minimum value of -170 nT one hour before midnight on the 20th, about the same time as the flow pressure falls to zero. The IMF continues to be southward for another 24 hours, but the recovery of the storm has already begun as the Dst is slowly recovering back to zero.

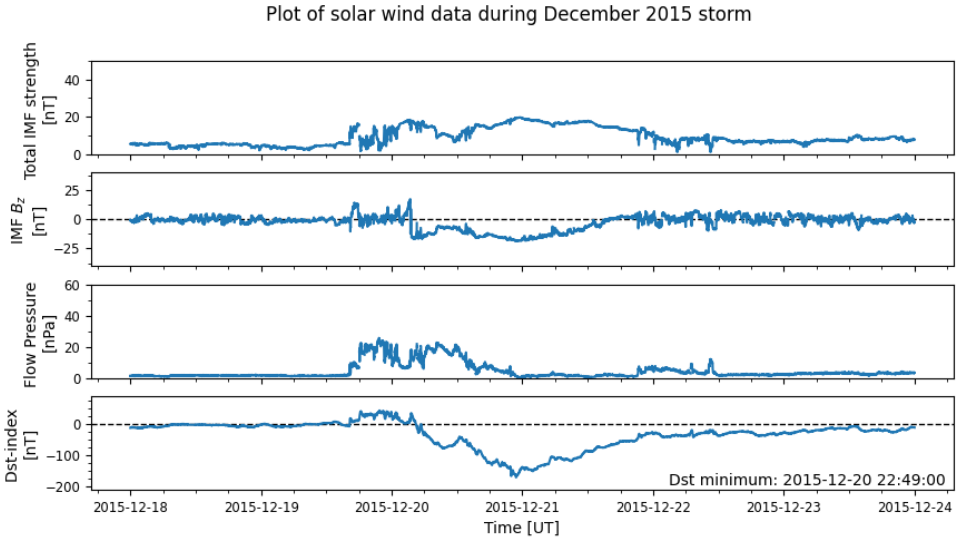

Figure 4.3: Solar wind data during the December 2015 storm. The first plot shows the magnitude of the IMF. The second shows the z-component of the IMF. The third shows the flow pressure. Lastly, the Dst-index is plotted. The bottom right corner shows the timestamp for when the Dst-index is at its lowest.

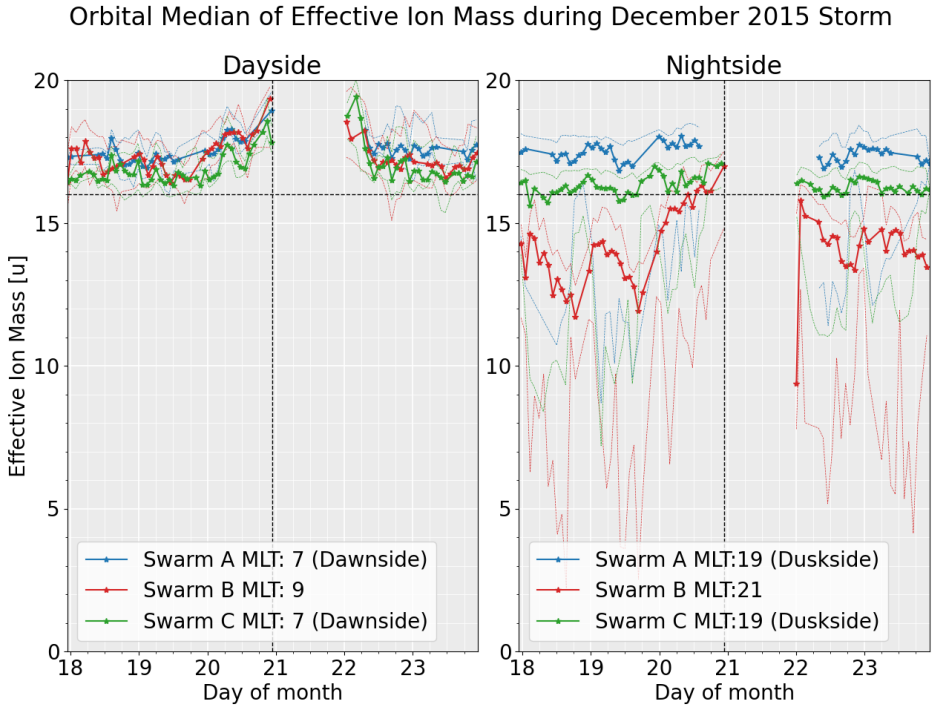

Figure 4.4: The orbital median of the Effective Ion Mass for the December 2015 storm. The figure contains one plot with dayside values and one for nightside. The dashed colored lines represent the 25/75 percentile of the M_{eff}. Time, expressed in the day of the month, is shown on the x-axis, and effective ion mass on the y-axis. The vertical dotted line shows the time of the storm's Dst-minimum, and the dotted horizontal line equals the mass of an oxygen ion, 16 u.

The time series of the effective ion mass during the December 2015 storm is shown in figure (4.4). It is important to notice that during this storm Swarm A and B have a dawn to dusk orbit, and there is no data available of the SLIDEM product for any of the satellites on the 21st of December, the day following the Dst-minimum. The dawnside values have been included in the dayside plot while the duskside values are plotted on the nightside. On the dayside, all three satellites measured similar values throughout the storm. The first two days the values stayed between 16-18 u, with Swarm A showing slightly higher values, about 1 u, than Swarm C. A day prior to the Dst-minimum there is a slight increase in effective mass recorded by all three satellites on the dayside, but this increase is only recorded by Swarm B on the nightside. The other two satellites show only minor fluctuations at the duskside throughout the six days. Again, Swarm A records values approximately 1 u above Swarm C, with an effective mass between 17-18 u and 16-17 u. Swarm B shows large fluctuations the first couple of days, alternating between 12 and 15 u. The first orbit after the data gap shows a large drop to less than 10 u, but it jumps back to approximately 16 u the following orbit. For the remaining part of the storm, Swarm B shows a slight decrease fluctuating between 13-15 u.

4.4 September 2017 Storm

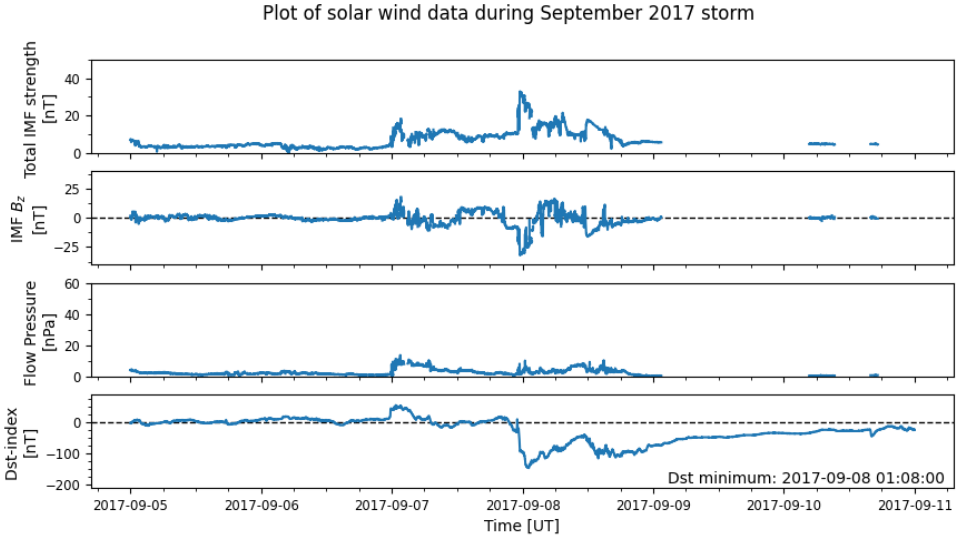

Figure 4.5: Solar wind data during the September 2017 storm. The first plot shows the magnitude of the IMF. The second shows the z-component of the IMF. The third shows the flow pressure. Lastly, the Dst-index is plotted. The bottom right corner shows the timestamp for when the Dst-index is at its lowest.

The OMNI data (figure 4.5) shows that there is an increase in the solar wind one day prior to the storm's SSC. An increase in flow pressure and magnitude makes an impact on the Dst-index, but as B_z is mostly positive the change in Dst is also positive. The solar wind calms down a little in the following hours until there is a sudden change in IMF strength, B_z, and Dst right before midnight to the 8th of September. The SSC can be spotted, and the storm reaches its minimum Dst value one hour after midnight. For the next 12 hours, the storm recovers, but at midday, there is another reduction in Dst accompanied by a negative B_z value and a small increase in flow pressure. Data is missing from the OMNI data set on the 9th, but as the Dst slowly recovers back to zero

during this time, it is safe to assume that the solar wind has calmed.

Figure (4.6) shows the time series of the effective ion mass during the September 2017 storm. None of the satellites have data recorded on the 8th of September, the day during and after the Dst-minimum. On the dayside, all three satellites record roughly the same measurements throughout the entire storm. The mass fluctuates slightly between 16-18 u. About two days after the Dst-minimum, the effective mass decreases to 14-15 u. On the nightside, Swarm A and C show similar data, while Swarm B records significantly lower values. On the first day (5th of September), Swarm A and B show a slow decrease in effective mass starting at 13-15 u down to 10-12 u. Swarm B starts with one orbit measuring 7.5 u but then falls to a stable value between 2.5-4 u the next two days. All three satellites experience an increase in the effective mass the day before the Dst-minimum. After the day of no recorded data, the effective mass is still above the pre-storm data, with 14-16 u for Swarm A and C, and 4-6 u for Swarm C. Alike the dayside plot, there is a decrease in effective mass for all three satellites about 48 hours after the Dst-minimum.

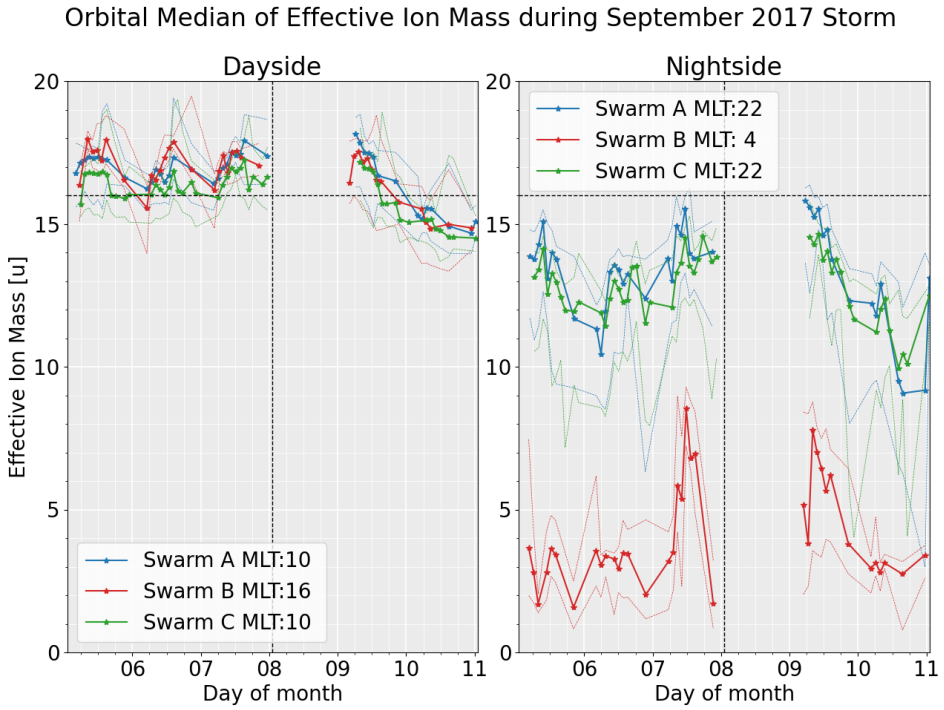

Figure 4.6: The orbital median of the Effective Ion Mass for the September 2017 storm. The figure contains one plot with dayside values and one for nightside. The dashed colored lines represent the 25/75 percentile of the M_{eff}. Time, expressed in the day of the month, is shown on the x-axis, and effective ion mass on the y-axis. The vertical dotted line shows the time of the storm's Dst-minimum, and the dotted horizontal line equals the mass of an oxygen ion, 16 u.

4.5 August 2018 Storm

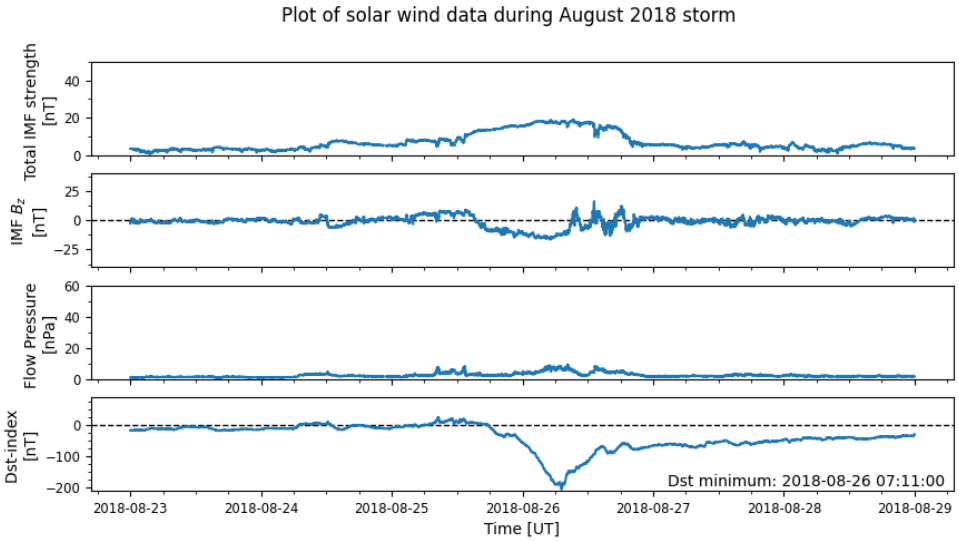

Figure 4.7: Solar wind data during the August 2018 storm. The first plot shows the magnitude of the IMF. The second shows the z-component of the IMF. The third shows the flow pressure. Lastly, the Dst-index is plotted. The bottom right corner shows the timestamp for when the Dst-index is at its lowest.

The August 2018 storm is the only of the four storms that have no clear SSC and is the storm with the lowest overall flow pressure (figure 4.7). In this case, the OMNI data shows a steady increase in the IMF's strength starting approximately 48 hours prior to the minimum Dst value. However, the z-component remains mostly small or positive until the afternoon of the 25th. At this point it stays negative for almost a day and then fluctuates between being positive or negative for another half a day. It is during this time the storm reaches its lowest value in Dst, -207 nT, at 07:00 on the 26th. During the fluctuations in B_z, two bumps in the Dst-index can be seen. Finally, the storm reaches its recovery phase which lasts for several days after this.

Observing the plots of the August storm (figure 4.8) shows a distinct increase in the effective mass around the same time as the Dst-minimum of the storm. The effective mass detected by Swarm A and C prior to the storm fluctuates between 12-14 u on the dayside and between 1-4 u on the nightside. A sudden increase happens around midnight to the 26th when the satellites measure an effective mass between 16-18 u at the dayside and 12-14 u at the nightside. This is an increase of 4 u at the dayside and about 10 at the nightside. Swarm B shows a similar pattern with an effective mass between 6-8 u before the storm and reaches a maximum of 15 u at the dayside at about the same time as Swarm A and B. On the nightside, the value starts at approximately 3 u pre-storm and increases to a maximum of about 8 u right after the data gap. All three satellites show a steady decrease in the effective mass in the next few days. An important remark regarding these observations is that it is the only storm that contains some data from the day during and after the Dst-minimum. Swarm C's SLIDEM data shows that M_{eff} reaches a maximum approximately four hours after the Dst-minimum. This can be observed on both the dayside and nightside.

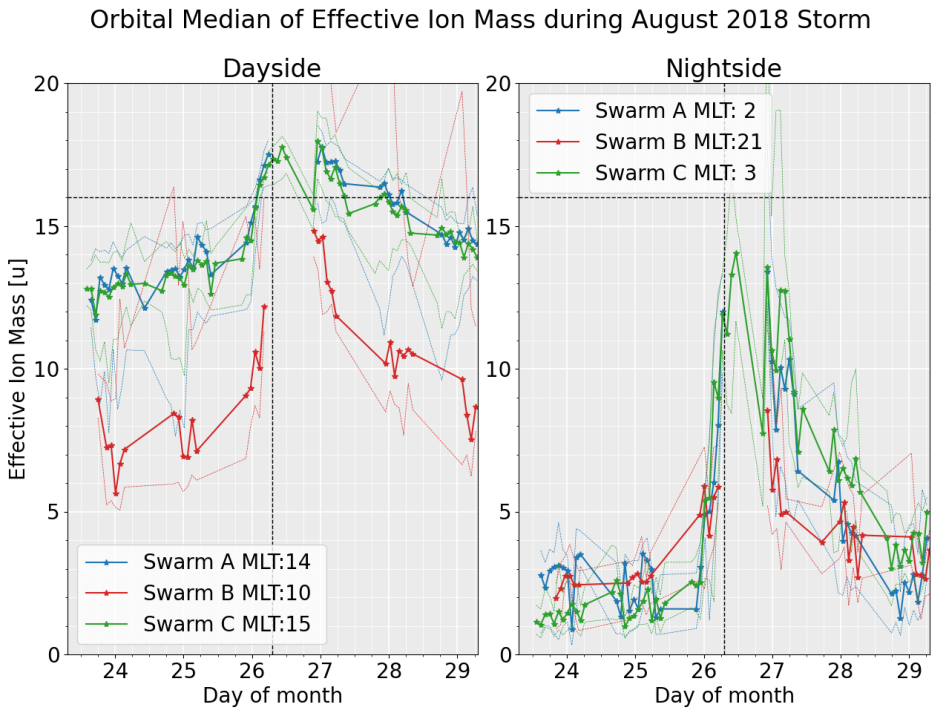

Figure 4.8: The orbital median of the Effective Ion Mass for the August 2018 storm. The figure contains one plot with dayside values and one for nightside. The dashed colored lines represent the 25/75 percentile of the M_{eff}. Time, expressed in the day of the month, is shown on the x-axis, and effective ion mass on the y-axis. The vertical dotted line shows the time of the storm's Dst-minimum, and the dotted horizontal line equals the mass of an oxygen ion, 16 u.

In this chapter, the observations done by the three Swarm satellites and the OMNI data have been presented for each storm. These were shown in two plots; one for the solar wind data and one for the effective ion mass. A table with baseline values based on data prior to each storm was shown at the beginning of this chapter (table (4.1)) and will be an important part of the discussion in the following chapter.

Chapter 5

Discussion

The main goal of this thesis is to investigate the changes in the ionospheric ion composition during a geomagnetic storm using the SLIDEM product. This chapter will include a discussion of the results in light of already established knowledge, a discussion of the methodology used in the thesis, and a discussion concerning the main question of the project.

The plots of the effective ion mass during the four storms are the main results to discuss in this section of the thesis. The SLIDEM product has provided a new and interesting method of investigating the changes to the ion composition in the ionosphere. In this section, these results will be discussed together with the solar wind data and baseline values. Later the methodology will be discussed.

First and foremost, an interesting problem occurs when looking at the different plots shown in the observations. According to previous studies of the ion composition of the ionosphere (Kelley, 2009; Prölss, 2010; Russell et al., 2016), the ion composition is believed to be mostly oxygen ions at the altitudes of the Swarm satellites. The effective ion mass plots of June 15, December 15, and September 17 all show an effective mass well above the mass of oxygen. This indicates the presence of heavier ions, but as the ionosphere composition figure (2.7) shows, heavier ions are only present up to an altitude of about 250 km. It is difficult to argue that even with the increased energy deposition into the ionosphere, molecular ions would reach the altitudes displayed by the SLIDEM product. Especially since the baseline values suggest the presence of heavier ions before the storm even kicked in (table (4.1)). It is difficult to pinpoint the exact reason for this but there might be an inaccuracy in the SLIDEM product or the Swarm measurements. However, the increased amount of O^+-ions would also lead to a larger amount of oxygen ions being removed through reaction with neutral N_2 and O_2 -molecules (reaction 2.12). Consequently, the existence of molecular ions, NO^+ and O_2^+, in Swarm altitude is possible(Gombosi, 1998). Nevertheless, the recombination of the heavier ions is a very fast reaction. It is in fact, 10^4 times quicker than the production of the molecular ions (Gombosi, 1998). Additionally, the percentage of NO^+ or O_2^+ needed to get an effective mass of 19 u is about 33 % of the total ion density (using equation (3.4) and assuming 0 % H^+), making this theory highly improbable.

The difference in the baseline values is another aspect to discuss. The June and December 2015 storms both show a baseline well above the oxygen ion mass (table (4.1)), while the September 17 and August 18 storms have baseline values around or below the oxygen mass. Comparing these values with the solar cycle could explain the differences in the offset of the baseline values. Figure (2.5) shows that the solar activity is decreasing during this period, with August 2018 close to the solar minimum. As solar activity is crucial for the structure of the ionosphere (Russell et al., 2016), it is reasonable to assume that solar activity could affect the calculated effective ion mass. This could potentially be the subject of further studies. Anyhow, more research will be necessary before anything can be concluded. Another reason for the difference in baselines could also be recent geomagnetic activity prior to the selected storm events. This is not an aspect taken into consideration in this thesis but is a possible error source. It could be an interesting facet to examine in a different study.

A deficiency in this thesis is the unavailability of important data. Especially data around the time of the Dst-minimum could have given significant insight into what happens during the peak of the storm. It would also be very interesting to look at the March 2015 storm, as it resulted in the lowest Dst-value of all the selected storms. There might be good reasons why the SLIDEM data set was unavailable for these dates. One reason could simply be that the ESA initiated protective measures to protect the satellites from increased solar wind activity, i.e. increasing the faceplate voltage. Additionally, a significant amount of data points had to be filtered out early in the analyzing process as the SLIDEM product was unable to calculate the effective mass, consequently defaulting the value to -1. A possible improvement could have been to increase the number of storms to study. It would be interesting to see if other storms in the solar minimum time frame would have shown similar results of the effective ion mass as the August 18 storm did.

Nevertheless, changes happening in the ion composition during a geomagnetic storm are still available to discuss. All four plots of effective ion mass show that there is an increase simultaneously with the main phase of the storms and a decrease during the recovery phase. The changes vary from storm to storm and whether you look at the nightside or dayside, but a tendency is possible to spot. This is an indication that the ion composition in the F-region of the ionosphere changes when impacted by a geomagnetic storm. Looking at the baseline plot for a quiet week (figure (3.3b)), there are still random fluctuations. One could argue that the changes are due to coincidences, but the fact that several of the twelve graphs suggest a change caused by a storm should imply otherwise.

Since the observations suggest an ion composition change, a natural area of discussion is how the changes in effective ion mass happen. It is already established that geomagnetic storms cause a large energy deposition into the Earth's magnetosphere and atmosphere (Prölss, 2010; Russell et al., 2016). The solar wind brings energy from the Sun to Earth in the form of radiation, IMF, and plasma. When the solar wind interacts with the magnetosphere, energy will deposit into the magnetosphere i.e. through charged particles becoming trapped in the ring current or plasma being moved into the polar regions through magnetic reconnection at the magnetotail (McPherron, 1995). The added energy could lead to an increase in the amount of ionized particles in the ionosphere. Potentially, at the altitude where the Swarm satellites orbit, more oxygen ions could be produced by the added energy, and the effective ion mass readings would increase.

Further, as the solar wind calms down, the increased amount of ions will not be sustainable, resulting in the oxygen ions either recombining into neutrals or sinking to lower altitudes (Gombosi, 1998). This would explain the decrease in the effective ion mass during the recovery phase, as the lighter ions would cover a larger part of the ion percentage.

Another aspect is the energy transportation from the polar regions to the lower latitudes. It is already well established that geomagnetic storms increase currents in the ionosphere and magnetosphere (Prölss, 2010; Russell et al., 2016). As much of this energy ends up in the polar regions, it will not affect the low-latitude ionosphere unless there is energy transportation leading to changes happening closer to the equatorial region. As described in section (2.8), studies show that traveling atmospheric disturbances (TAD) from the polar region move toward lower latitudes following a geomagnetic event. Prölss (2010) explains how the TAD originating from the north will encounter the TAD originating from the south leading to a superposition of the disturbances and causing the ionosphere to expand. This also corresponds with studies investigating the variations of the inner magnetosphere during a geomagnetic storm. These show that the ion composition changes from mainly H^+-ions ($\sim$ 15 % O^+) pre-storm to mainly O^+-ions ($\sim$ 75 % O^+) concurrent with the maximum epoch of the storm (Daglis et al., 1999). It further suggests that the oxygen ions originate from the ionosphere, hence a sign of a vertical expansion and transportation of ions to higher altitudes.

One more question to discuss is why the August 18 storm is somewhat different from the other three storms. The August storm plot (Figure (4.8)) shows a clear increase in the effective ion mass toward the Dst-minimum. One possible explanation can be found in the OMNI data. The recorded flow pressure is the lowest for this storm compared to the other three. This is probably the reason that this storm does not have a clear SSC, as the dayside magnetosphere does not get compressed as much. The B_z-component of the magnetic field also stays negative for a prolonged amount of time without any fluctuations. This was also observed in the December 15 storm, but here the flow pressure was significantly higher. Another explanation comes back to the different baseline values discussed earlier. As August 2018 is close to the solar minimum between solar cycles 24 and 25, the low radiation hitting the Earth's atmosphere could result in a higher density of lighter ions in the Swarm altitude of the ionosphere. When a larger event, like the August 18 storm, happens, the added energy deposited into the atmosphere could lead to a vertical expansion in the altitudes with oxygen ions. It is also the only storm that has SLIDEM data available during and after the Dst-minimum, but only for Swarm C. The peek in M_{eff} during this time period is about 4 hours after the Dst-minimum. This correlates well with the time it takes traveling atmospheric disturbances (TAD) to reach the equatorial region from their origin at the poles (Prölss, 2010). The TADs propagate outward from their source region covering the entire Earth, which fits with the observations in figure (4.8) as the peak in M_{eff} is observed simultaneously at the dayside and nightside. However, the lack of SLIDEM data during the storms' peaks makes it impossible to conclude, but this aspect might be interesting for future studies.

In this thesis, the SLIDEM data of the effective ion mass during four storms have been analyzed. Which storms to study were chosen based on the Dst-index and then compared with the K_p-index. This process was rather spontaneous and the election was not thoroughly thought through. Expectations that larger storms would reveal more interesting results, prompted the search for disturbances within the Dst-index. In hind-

sight, it would have been interesting to investigate a greater number of storms. (This has, however, been done in a recently published article that will be discussed in the next paragraph.) Especially because of the realization that the solar cycle potentially plays a significant role in the effective ion mass data. As only the December 2018 storm was during the solar minimum, it is ill-considered to conclude that there is a correlation based on the observations done in this thesis.

A study conducted by the creators of the SLIDEM product did a superposed epoch analysis across 4 years (2016-2020) of SLIDEM data investigating all storms with a Dst-value below -50 nT (Pakhotin et al., 2023). Of the four storms selected in this thesis, two of them, September 17 and August 18, fall within the time frame of this study. When comparing the observations (figure (4.6) and (4.8)) with the superposed epoch analysis of effective ion mass, the dayside of the August 18 storm and both the nightside observation correlates well with the superposed epoch results. The dayside of the September 17 storm display values above these results pre-storm, but show similarities when the storm enters its recovery phase in the days following the Dst-minimum. The article written by Pakhotin et al. (2023) was only recently published (24th of April 2023), hence it is not used to a greater extent in this thesis. It is, however, encouraging to see that results and observations from this thesis correlate with similar studies conducted on a larger data set.

Chapter 6

Conclusion and Outlook

The goal of this thesis has been to investigate the ionospheric composition changes during geomagnetic storms. The newly developed SLIDEM product has made it possible to use Swarm satellite data to get an overview of the effective ion mass and observe how it changes due to different circumstances, e.g. a geomagnetic storm. The data and observations presented and displayed in this thesis show a correlation between geomagnetic storms and the ionosphere ion composition, in line with established theory. Before the peak of the storm, the observations of the effective ion mass increase until it reaches a peak a few hours after the Dst-minimum. The recovery phase of the storm correlates well with the decrease in M_{eff} in the same period. It is, however, hard to conclude, as the chosen storms gave very different observations in baseline values making the results difficult to compare with each other.

Pakhotin et al. (2022) wanted their SLIDEM product to produce reliable data on the effective ion mass that could detect small variations in the lighter ion fraction. Observations presented in this thesis show that this is exactly what they have managed to do. However, it has been difficult to find an adequate explanation of why the M_{eff} shows values above 16 u, the mass of an oxygen ion. Probable reasons have been discussed, and especially the solar activity level seems to have an impact on high baseline values of M_{eff}.

The research done in this thesis has provided two implications for the field of space physics. It has shown that SLIDEM is a valid data product to use when investigating ionosphere composition at lower latitudes. Secondly, it has provided observations that support the established theory that a geomagnetic storm is a global event and will affect, not only the poles but, through energy transportation, all of Earth.

As a final statement, the SLIDEM product has proved to provide more detailed measurements of the ionosphere ion composition than just assuming 100 % O^+ or using models like the IRI-2016. The results of this thesis show that there is a correlation between a geomagnetic storm and a larger fraction of heavy ions in the ionosphere.

6.1 Outlook

As this thesis comes to an end, some suggestions for further studies will be presented. Firstly, further studies of ion composition changes in the ionosphere using the SLIDEM product could include data from a larger number of storms, as this would increase the reliability of the results. It would also be interesting to find storms that have available data for the entire duration of the storm without the 24-hour gap, which was present in most of the data in this thesis. If more data shows a peak in the M_{eff} a few hours after the Dst-minimum, this could strengthen the theory of TADs causing the increase. Making sure to include storms from several different stages of the solar cycle could also be an important contribution to increased knowledge of the ionosphere composition.

Another idea would be to include the density measurements provided by the SLIDEM product as a measure of comparison for different storms. This could provide some insights into the offsets between the baseline values. As seen in the results, much of the data suggests an effective ion mass well above 16 u, which is not in line with established knowledge. If this is the case for other similar studies, investigating potential inaccuracies in the SLIDEM product may be necessary.

Bibliography

Appleton, E. V. (1946). Two Anomalies in the Ionosphere. *Nature*, *157*(3995), 691–691. https://doi.org/10.1038/157691a0

Battrick, B. (Ed.). (2004). *Swarm - The Earth's Magnetic Field and Environment Explorers* (tech. rep. ESA SP-1279(6)). European Space Agency. https://esamultimedia.esa.int/docs/SP_1279_6_Swarm.pdf

Bruevich, E., & Bruevich, V. (2019). Long-term trends in solar activity. Variations of solar indices in the last 40 years [Publisher: National Astronomical Observatories, CAS and IOP Publishing Ltd.]. *Research in Astronomy and Astrophysics*, *19*(7), 090. https://doi.org/10.1088/1674-4527/19/7/90

Burchill, J. K., Pakhotin, I. P., Förster, M., & Lomidze, L. (2022). Swarm lp ion drift and effective mass product definition. https://swarm-diss.eo.esa.int/#swarm/Advanced/Plasma_Data/2_Hz_Ion_Drift_Density_and_Effective_Mass_dataset

Cander, L. R., & Mihajlovic, S. J. (1998). Forecasting ionospheric structure during the great geomagnetic storms. *Journal of Geophysical Research: Space Physics*, *103*(A1), 391–398. https://doi.org/10.1029/97JA02418

Chen, F. F. (2016). *Introduction to Plasma Physics and Controlled Fusion*. Springer International Publishing. https://doi.org/10.1007/978-3-319-22309-4

Daglis, I. A., Kasotakis, G., Sarris, E. T., Kamide, Y., Livi, S., & Wilken, B. (1999). Variations of the ion composition during an intense magnetic storm and their consequences. *Physics and Chemistry of the Earth, Part C: Solar, Terrestrial & Planetary Science*, *24*(1), 229–232. https://doi.org/https://doi.org/10.1016/S1464-1917(98)00033-6

Darian, D., Marholm, S., Paulsson, J. J. P., Miyake, Y., Usui, H., Mortensen, M., & Miloch, W. J. (2017). Numerical simulations of a sounding rocket in ionospheric plasma: Effects of magnetic field on the wake formation and rocket potential [_eprint: https://agupubs.onlinelibrary.wiley.com/doi/pdf/10.1002/2017JA024284]. *Journal of Geophysical Research: Space Physics*, *122*(9), 9603–9621. https://doi.org/https://doi.org/10.1002/2017JA024284

Dungey, J. W. (1961). Interplanetary Magnetic Field and the Auroral Zones [Publisher: American Physical Society]. *Phys. Rev. Lett.*, *6*(2), 47–48. https://doi.org/10.1103/PhysRevLett.6.47

ESA. (2023). Swarm Data Access. Retrieved April 21, 2023, from https://swarm-diss.eo.esa.int/#swarm/Advanced/Plasma_Data/2_Hz_Ion_Drift_Density_and_Effective_Mass_dataset

Friis-Christensen, E., Lühr, H., Knudsen, D., & Haagmans, R. (2008). Swarm – An Earth Observation Mission investigating Geospace. *Advances in Space Research*, *41*(1), 210–216. https://doi.org/10.1016/j.asr.2006.10.008

Ganushkina, N. Y., Liemohn, M. W., Dubyagin, S., Daglis, I. A., Dandouras, I., De Zeeuw, D. L., Ebihara, Y., Ilie, R., Katus, R., Kubyshkina, M., Milan, S. E., Ohtani, S., Ostgaard, N., Reistad, J. P., Tenfjord, P., Toffoletto, F., Zaharia, S., & Amariutei, O. (2015). Defining and resolving current systems in geospace. *Annales Geophysicae*, *33*(11), 1369–1402. https://doi.org/10.5194/angeo-33-1369-2015

Garner, R. (2015). Solar Storm and Space Weather. Retrieved May 2, 2023, from http://www.nasa.gov/mission_pages/sunearth/spaceweather/index.html

GFZ. (2023). Kp daily plots - Kp index. Retrieved April 27, 2023, from https://kp.gfz-potsdam.de/en/figures/kp-daily-plots

Gombosi, T. I. (1998). The Ionosphere. In *Physics of the Space Environment* (pp. 176–208). Cambridge University Press. https://doi.org/10.1017/CBO9780511529474.011

Jordan, A. (2023). Kp Index. Retrieved April 29, 2023, from https://www.gfz-potsdam.de/en/section/geomagnetism/data-products-services/geomagnetic-kp-index

Kelley, M. (2009). *The Earth's Ionosphere: Plasma Physics and Electrodynamics*. Elsevier Science. https://books.google.no/books?id=3GlWQnjBQNgC

King, J., & Papitashvili, N. (2008). One min and 5-min solar wind data sets at the Earth's bow shock nose. Retrieved April 19, 2023, from https://omniweb.gsfc.nasa.gov/html/omni_min_data.html

Knudsen, D. J., Burchill, J. K., Buchert, S. C., Eriksson, A. I., Gill, R., Wahlund, J.-E., Åhlen, L., Smith, M., & Moffat, B. (2017). Thermal ion imagers and Langmuir probes in the Swarm electric field instruments [_eprint: https://onlinelibrary.wiley.com/doi/pdf/10.1002/2016JA022571]. *Journal of Geophysical Research: Space Physics*, *122*(2), 2655–2673. https://doi.org/10.1002/2016JA022571

Lyons, L. (2003). Space Plasma Physics. In R. A. Meyers (Ed.), *Encyclopedia of Physical Science and Technology (Third Edition)* (Third Edition, pp. 577–591). Academic Press. https://doi.org/https://doi.org/10.1016/B0-12-227410-5/00716-X

Matzka, J., Stolle, C., Yamazaki, Y., Bronkalla, O., & Morschhauser, A. (2021). The Geomagnetic Kp Index and Derived Indices of Geomagnetic Activity [_eprint: https://onlinelibrary.wiley.com/doi/pdf/10.1029/2020SW002641]. *Space Weather*, *19*(5), e2020SW002641. https://doi.org/10.1029/2020SW002641

Mayaud, P. (1980). *Derivation, Meaning, and Use of Geomagnetic Indices* (1st ed.). American Geophysical Union (AGU). Retrieved April 30, 2023, from https://agupubs.onlinelibrary.wiley.com/doi/10.1029/GM022

McPherron, R. (1995). Magnetospheric dynamics. In *Introduction to Space Physics* (pp. 400–458). Cambridge University Press. http://www.igpp.ucla.edu/public/rmcpherr/McPherronPDFfiles/McPherron_Chapter13_KandR.pdf

Nakariakov, V. M., Pilipenko, V., Heilig, B., Jelínek, P., Karlický, M., Klimushkin, D. Y., Kolotkov, D. Y., Lee, D.-H., Nisticò, G., Van Doorsselaere, T., Verth, G., & Zimovets, I. V. (2016). Magnetohydrodynamic Oscillations in the Solar Corona and Earth's Magnetosphere: Towards Consolidated Understanding. *Space Science Reviews*, *200*(1-4), 75–203. https://doi.org/10.1007/s11214-015-0233-0

NASA. (2006). The History of Auroras [Publisher: Brian Dunbar]. Retrieved May 7, 2023, from http://www.nasa.gov/mission_pages/themis/auroras/aurora_history.html

NASA. (2014). The Solar Wind. Retrieved May 2, 2023, from https://solarscience.msfc.nasa.gov/SolarWind.shtml

NOAA. (2021). Earth from Orbit: Gravity Waves. Retrieved May 8, 2023, from https://www.nesdis.noaa.gov/news/earth-orbit-gravity-waves

Pakhotin, I. P., Burchill, J. K., Förster, M., & Lomidze, L. (2022). The swarm langmuir probe ion drift, density and effective mass (SLIDEM) product. *Earth, Planets and Space*, *74*(1). https://doi.org/10.1186/s40623-022-01668-5

Pakhotin, I. P., Burchill, J. K., Förster, M., & Lomidze, L. (2023). Light ion dynamics in the topside ionosphere and plasmasphere during geomagnetic storms. *Earth, Planets and Space*, *75*(1), 62. https://doi.org/10.1186/s40623-023-01818-3

Parsec. (2023). Top 50 geomagnetic storms of 2015. Retrieved April 16, 2023, from https://www.spaceweatherlive.com/en/auroral-activity/top-50-geomagnetic-storms/year/2015.html

Pecseli, H. L. (2020). *Waves and Oscillations in Plasmas* (2nd ed.). CRC Press. https://doi.org/10.1201/9780429489976

Priest, E., & Forbes, T. (2000). *Magnetic Reconnection: MHD Theory and Applications*. Cambridge University Press. https://doi.org/10.1017/CBO9780511525087

Prölss, G. W. (2010). *Physics of the earth's space environment: An introduction* [OCLC: 968554506]. Springer.

Resendiz Lira, P. A., & Marchand, R. (2021). Simulation Inference of Plasma Parameters From Langmuir Probe Measurements. *Earth and Space Science*, *8*(3), e2020EA001344. https://doi.org/10.1029/2020EA001344

Resendiz Lira, P. A., Marchand, R., Burchill, J., & Förster, M. (2019). Determination of Swarm Front Plate's Effective Cross Section From Kinetic Simulations. *IEEE Transactions on Plasma Science*, *47*(8), 3667–3672. https://doi.org/10.1109/TPS.2019.2915216

Rishbeth, H. (1981). The F-region dynamo. *Journal of Atmospheric and Terrestrial Physics*, *43*(5), 387–392. https://doi.org/https://doi.org/10.1016/0021-9169(81)90102-1

Russell, C. T., Luhmann, J. G., & Strangeway, R. J. (2016). *Space physics: An introduction*. Cambridge University Press. https://doi.org/10.1017/9781316162590

Smirnov, A., Shprits, Y., Zhelavskaya, I., Lühr, H., Xiong, C., Goss, A., Prol, F. S., Schmidt, M., Hoque, M., Pedatella, N., & Szabó-Roberts, M. (2021). Intercalibration of the plasma density measurements in earth's topside ionosphere. *Journal of Geophysical Research: Space Physics*, *126*(10), e2021JA029334. https://doi.org/https://doi.org/10.1029/2021JA029334

Sugiura, M. (1991). Dst-index. Retrieved April 30, 2023, from https://wdc.kugi.kyoto-u.ac.jp/dstdir/dst2/onDstindex.html

SuperDARN. (2023). Tutorials :: Plasma Environment. Retrieved May 6, 2023, from https://superdarn.ca/tutorials-14

Truhlik, V., Bilitza, D., & Triskova, L. (2015). Towards better description of solar activity variation in the International Reference Ionosphere topside ion composition model. *Advances in Space Research*, *55*(8), 2099–2105. https://doi.org/10.1016/j.asr.2014.07.033

Vallée, J. (1998). Observations of the Magnetic Fields. *Fundamentals of Cosmic Physics*, *19*, 319–422. https://ned.ipac.caltech.edu/level5/March03/Vallee2/paper.pdf

Wood, A. G., Alfonsi, L., Clausen, L. B. N., Jin, Y., Spogli, L., Urbář, J., Rawlings, J. T., Whittaker, I. C., Dorrian, G. D., Høeg, P., Kotova, D., Cesaroni, C., Cicone, A., Miedzik, J., Gierlach, E., Kochańska, P., Wojtkiewicz, P., Shahtahmassebi, G., & Miloch, W. J. (2022). Variability of Ionospheric Plasma: Results from the ESA

Swarm Mission. *Space Science Reviews*, *218*(6), 52. https://doi.org/10.1007/s11214-022-00916-0

Woodman, R. F., & La Hoz, C. (1976). Radar observations of F region equatorial irregularities. *Journal of Geophysical Research (1896-1977)*, *81*(31), 5447–5466. https://doi.org/https://doi.org/10.1029/JA081i031p05447

Appendix A

The Python Code

All Python programs used to analyze the SLIDEM and OMNI data in this thesis can be found on GitHub:
https://github.com/mahelvig/Master-Real